Journal Pre-proofs

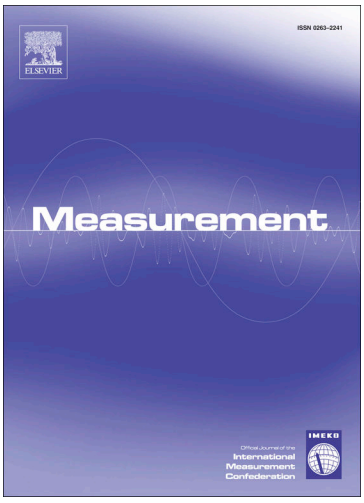

Damage detection in plates based on Lamb wavefront shape reconstruction

Beata Zima

PII: S0263-2241(21)00223-2
DOI: https://doi.org/10.1016/j.measurement.2021.109206
Reference: MEASUR 109206

To appear in: *Measurement*

Received Date: 17 October 2020
Revised Date: 16 February 2021
Accepted Date: 18 February 2021

Please cite this article as: B. Zima, Damage detection in plates based on Lamb wavefront shape reconstruction, *Measurement* (2021), doi: https://doi.org/10.1016/j.measurement.2021.109206

Damage detection in plates based on Lamb wavefront shape reconstruction

Beata Zima

Department of Structural Mechanics
Faculty of Civil and Environmental Engineering
Gdańsk University of Technology
ul. Narutowicza 11/12, 80-233 Gdańsk, Poland
email: beata.zima@pg.edu.pl

Abstract

Many of the current studies in the area of damage detection using elastic wave propagation are based on deploying sensor networks with a large number of piezoelectric transducers to detect small-size cracks. A major limitation of these studies is that cracks are usually larger and have different shapes in real cases. Moreover, using a large number of sensing nodes for damage detection is both costly and computationally intensive. The paper proposes a novel elastic wave propagation method for damage detection based on the reconstruction of the shape of the reflected wavefront. The main advantage of the developed approach is that merely three sensors are necessary to localize and estimate the size of the cracks with various sizes and shapes. Several damage cases with different number of piezoelectric transducers and placement have been investigated experimentally. Extensive numerical simulations are performed to benchmark the performance of the proposed method.

Keywords:

damage detection; guided waves; crack, plate, transducers configuration, wavefront

1. Introduction

Guided waves, because of the high potential of damage detection have received tremendous attention in the field of Structural Health Monitoring (SHM) and Nondestructive Testing (NDT) [1]-[9]. The capacity to travel long distances with relatively low amplitude decay and the sensitivity to various defect types causes that guided waves are especially attractive for plate-like structures diagnosis ([10],[11]). In the last years, the research on the development of wave-based methods for damage detection in plate-like structures has been carried out in many different directions. A procedure for locating and estimating the extent of linear cracks in aluminum plates was proposed by Tua *et al*. [12]. A phased array of piezoelectric transducers and an ellipse-based method for point-damage detection in metallic plates was used by Wandowski *et al*. [13] and Radzieński *et. al.* [14]. A weighted sparse reconstruction-based method for small size damages in the composite plate has been proposed by Xu et al. [15]. Zhang et al. [16] used a multiple sparse Bayesian learning approach and ellipse-based method to visualize the damage in composite plates. The three-stage algorithm combination of detection theory and array processing frameworks capable to extract locations of multi-damage in plate-like structures has been described by Bahador et al. [17]. Mori et al. [18] developed damage detection and localization method for plate structures using the time-reversal method and mode-converted Lamb waves. A neural network-based damage localization method was proposed by Zhang et al. [19]. The damage identification algorithm using improved 2D multiple signal classification (MUSIC) has been described by Zou [20]. Huang et al. [21] developed the baseline-free damage detection in composite plates using edge-reflected Lamb waves. The soft-thresholding process, based on discrete wavelet transform and the empirical mode decomposition was introduced by Wang *et al*. [22] to damage identification in a plate. The processing algorithm proposed by Liu *et al*. [23] was based on signal filtering registered by 16 transducers in a compact rectangular phased array.

In the majority of the reported papers, the ellipse method based on the time of flight was used to localize the damage in plate-like structures. This method requires the network of at least three sensors to unambiguously localize the small-size damage however, usually the more extensive sensor network was incorporated to improve the quality of damage maps. The ellipse-based method was usually used for localizing the damages or notches however, it did not allow to determine the type of damage (point-like damage, line-cracks, large-size surface damage, etc.) as well as to estimate its size. The attempts of crack size estimation using the ellipse-based method have been presented in [24]. It was proved that for each transducers configuration exists a detectable limit length of the crack. Damage quantitative evaluation using Lamb waves and

ellipse-based method has been presented by Hua et al. [25]. They proposed the modified imaging method and extended the dictionary construction to damages with any size and shape. The sparse Bayesian learning was employed for Lamb wave damage imagining by Zhang et al. [26]. Based on the obtained damage maps the size of the damage can be roughly estimated.

Despite numerous papers dealing with damage localization using Lamb waves, the exact estimation of its size remains a challenge. Moreover, there is a need to develop methods that would allow for recognizing the type of damage. This article presents the novel method of line-damage size detection and size determination based on the reconstruction of the curvature of the reflected wavefront enhanced with the ellipse-based method. The paper proves that the type of damage influences the radius as well as the amplitude of the reflected wavefront, which is the main idea of the novel method. Based on the theoretical distance-amplitude relationship derived using the dispersion compensation method, the damage zone from which the wave was reflected can be unambiguously identified. In the proposed approach the network of only three sensors is required to detect and estimate the size of the line crack, which so far was the minimum number to detect the small-size damage. A significant reduction in the number of sensors results in the reduction in the costs of the entire monitoring system, reducing the number of recorded signals and in consequence the shortening of the analysis time. The detection algorithm is described step by step. Its diagnostic abilities have been verified numerically and experimentally for various transducers configurations. Both advantages and limitations of the proposed approach are faithfully discussed.

2. The analysis of the relation between wave amplitude and the propagation path length

The attenuation of Lamb waves is a commonly used feature of guided waves for SHM and NDT purposes ([27],[28]). It is a critical parameter in the selection of an appropriate wave mode for long-range inspection. The two main factors influencing the intensity of wave attenuation is geometry and material properties. As a wave propagates in a plate-like structure, the radius of the wavefront increases and the amplitude decays. Moreover, because of the dispersive nature of guided waves, the wave packet spreads and changes its shape, which also affects the signal amplitude. The possible additional interactions with damaged regions or obstacles often resulting in mode conversions influence the amplitude. This type of attenuation neglects the energy dissipation, which is caused by the material's viscoelastic properties. In the real case, the reduction in amplitude is due to both, geometric and material attenuation. The exponential decay of Lamb wave with amplitude , propagating with group velocity v_g and A_1 for excitation frequency *f* after traveling a distance Δx is described by the following equation ([29],[30]):

$$A_2 = A_1 e^{-\kappa \Delta x}. \tag{1}$$

where A_2 is the amplitude registered in distance Δx and the parameter κ can be calculated as:

$$\kappa = \frac{f\xi}{v_g}. \tag{2}$$

and ξ is structural damping. The exponent contains the components related to both geometric attenuation (Δx) and material attenuation (ξ). The above equation was used by Ramadas et al. [30] to model the damping of Lamb waves in composite plates. Their investigation proved the correctness of the relationship, but the measurements were made for relatively small distances (<90 mm). The relationship between Lamb wave amplitude and distance from the excitation source was derived in [31] based on Dispersion Compensation Method (DCM). The following section contains the theoretical, numerical, and experimental analysis of the relationship between Lamb wave amplitude and length of the propagation path with taking into account wave reflections from various crack zones (end and middle points).

2.1 Dispersion Compensation Method

Dispersion Compensation is a commonly used processing method allowing for suppressing the dispersion effects by making use of known a priori the dispersion curves of the investigated structure ([32],[33]). It provides information about the time variability of the guided wave *u*(*r*,*t*) however, it does not allow to predict the amplitude changes, which is a

serious limitation of this approach. According to DCM the Lamb wave response $u(r,t)$ at the distance r from the source and after the time t takes the following form:

$$u(r,t) = \int_{-\infty}^{\infty} F(\omega) e^{j[\omega t - k(\omega) r]} d\omega . \tag{3}$$

where $F(\omega)$ is the Fourier transform of the excitation function and $k(\omega)$ is angular frequency versus wavenumber dependency. In this study, the perfect, isotropic plate with constant thickness h is considered. The relationship between wavenumber and frequency can be obtained by solving Lamb-Rayleigh dispersion equations:

$$\frac{\tan(qh)}{\tan(ph)} = -\frac{4k^2 pq}{\left(k^2 - q^2\right)^2} . \tag{4}$$

$$\frac{\tan(qh)}{\tan(ph)} = -\frac{\left(k^2 - q^2\right)^2}{4k^2 pq} . \tag{5}$$

The parameters p and q are described as follows:

$$p^2 = \frac{\omega^2}{c_L^{\,2}} - k^2 . \tag{6}$$

$$q^2 = \frac{\omega^2}{c_T^{\,2}} - k^2 . \tag{7}$$

where c_T and c_L are the velocities of transverse and longitudinal waves in an infinite medium, respectively. Equation (4) describes the dispersion relation for symmetric modes, while Eq. (5) concerns antisymmetric modes. To overcome the limitations of DCM related to the lack of information about the amplitude, the fundamental DCM equation must be modified. Because the discussed problem relates to the wave propagation in isotropic and homogeneous plate-like structure, after excitation wave travels with the same velocity in all directions. Thus, the shape of the wavefront is circular. If we consider the plate structure as a closed system, where the transfer of energy is not allowed, the total energy measured on the increasing wavefront circuit must be constant at any time. Therefore, the total energy E of the system can be described by the following relationship:

$$E = \int_{-\infty}^{\infty} 2\pi r \, U(r,t)^2 \, dt = const . \tag{8}$$

where $U(r,t)$ is the shape of the propagating disturbance at a distance r from the excitation source. Because the energy calculated using DCM (Eq. (3)) or based on Lamb dispersion equations (Eq. (8)) must be the same, one can write:

$$2\pi r\, U(r,t)^2 = u(r,t)^2 . \tag{9}$$

After substituting Eq. (3) into Eq. (9) and some modifications, the relationship describing the shape of the propagating disturbance takes the following form:

$$U(r,t) = \frac{1}{\sqrt{2\pi r}} \int_{-\infty}^{\infty} F(\omega) e^{j[\omega t - k(\omega) r]} d\omega . \tag{10}$$

In the above relationship, the amplitude attenuation caused by energy dissipation is omitted. To include the influence of material damping, the Eq. (10) is additionally multiplied by the exponential factor $e^{-r\xi_s}$, where r is the length of the propagation path and ξ_s the damping parameter:

$$U(r,t) = \frac{e^{-r\xi_s}}{\sqrt{2\pi r}} \int_{-\infty}^{\infty} F(\omega) e^{j[\omega t - k(\omega) r]} d\omega . \tag{11}$$

Because the transducers are usually attached at the plate surface and the excitation is applied perpendicularly, the relation $k(\omega)$ occurring in Eq. (11) is determined only for antisymmetric modes.

2.2 Experimental investigation of amplitude and propagation path length relationship

In the next stage, the experimental amplitude-distance curve was determined and compared with the theoretical predictions summarized in the previous section. All results presented in the paper concern the excitation frequency of 100 kHz. For this frequency, the signals were characterized by the relatively high amplitude and readability, which significantly improved the interpretation of the results. Although the paper presents the results for one frequency, the theoretical reasoning presented in the further part of the study is valid also for other parameters of the excitation. To excite the antisymmetric mode the sensors and actuator were attached perpendicularly. Thus the poling direction was perpendicular to the plate surface. Because the sensors and actuators were attached perpendicularly on the plate surface, mainly antisymmetric mode was excited. Based on the dispersion equations ([34],[35]) for the frequency of 100 kHz only one antisymmetric mode A0 can be excited, and therefore all further considerations concerns this wave mode. The compressive-type transducers Noliac NAC2012 were mounted on a plate surface by wax. The dimensions of the transducers were 3 mm × 3 mm × 2 mm. The maximum operating voltage was 100 V. A free stroke was 3.3 μm and a blocking force was 378 N.

Because the signal amplitude registered by the transducers strongly depends on several factors like quality of the attachment or wax temperature, the amplitude measurement required

a special approach. The procedure of amplitude measurement is explained step by step in Figure 1. The actuator was attached perpendicularly near the edge of the plate. The sensor capturing the signal was attached at a greater distance from the boundary. After wave excitation, the sensor registered the incident wave first and then the reflection from the edge. The amplitudes of envelopes $A_1(d)$ and $A(2c+d)=A(r_1)$ measured at the distances d and ($2c$+d) were determined, respectively (Figure 1). In general, the dissipation of energy after reflection from the plate edge is insignificant and therefore was neglected. Next, the sensor-actuator configuration was rearranged. The next configurations were designed so that one of the amplitude was measured at the same distance as in the previous case (d or c). This approach allowed for referencing and normalizing the results with respect to each other. The solution presented in Figure 1 involved the signal measurement at the distance $A_2(d)$ and $A(2e+d)=A(r_2)$. The normalization process involves determining the ratio n, which is a quotient of amplitudes $A_1(d)$ and $A_2(d)$:

$$n=\frac{A_1(d)}{A_2(d)}. \tag{12}$$

Next, the amplitude of reflection from the plate edge registered at the distance ($2e$+d) was normalized:

$$A'(r_2)=nA(r_2). \tag{13}$$

In this way, the mutual relationship between the amplitudes measured at the distances d, r_1 and r_2 was obtained. In the next stage, the configuration of the transducer was rearranged again and the relationships between the amplitudes for the different propagation path lengths were determined. The amplitude value has been determined for distances from 1 cm to 10 cm with step 1 cm, 15 cm and from 20 cm to 60 cm with step 10 cm from the excitation source. The experimental and theoretical results are presented in Figure 2. The theoretical curve described by Eq. (11) was calculated for the damping coefficient ξ = 0.335 [1/m], which was established by the systematic search method. The high agreement of the results is visible, which proves the correctness of the theoretical distance-amplitude relationship. The knowledge of the distance-amplitude curve allows for the prediction of the exact amplitude at any distance from the excitation source but also on determining the propagated distance only based on the amplitude value, which usually could be determined only based on the ToF and wave velocity.

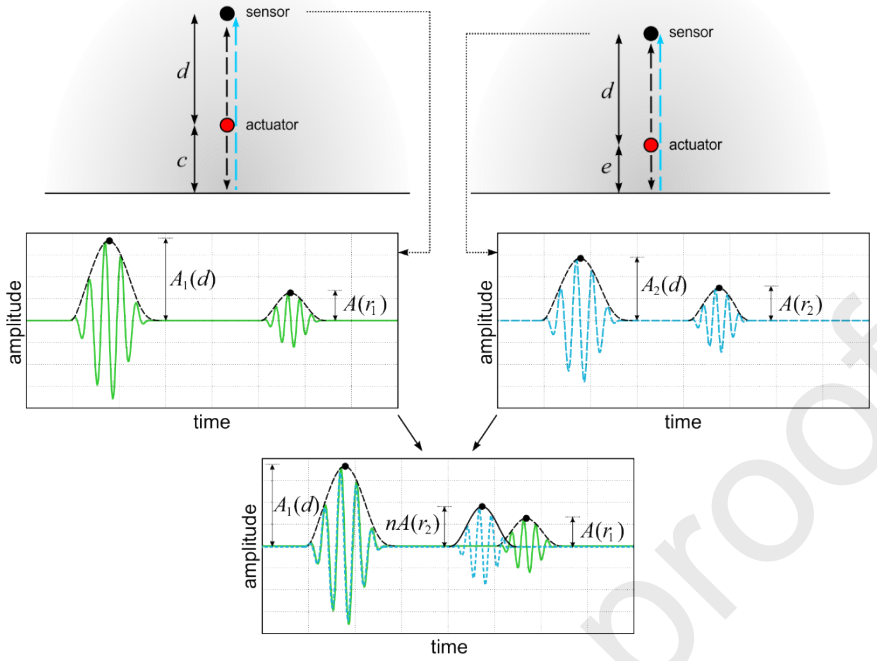

Figure 1 The scheme of the procedure of experimental wave amplitude measurement

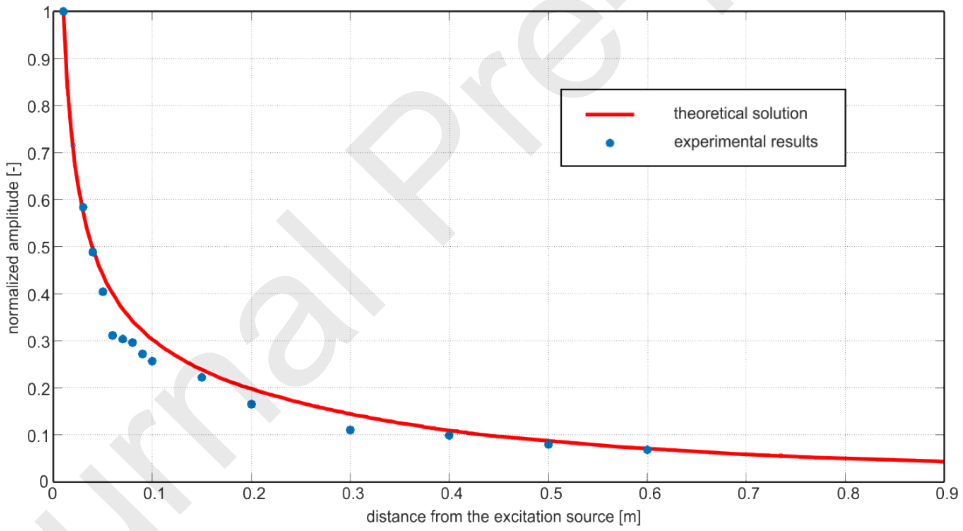

Figure 2 Amplitude-distance curve: comparison of theoretical and experimental results

2.3 Wave interaction with damages

The above derivations were made for disturbance, which propagates through undamaged regions and the amplitude is affected only by the increasing traveled distance and the material damping. However, the amplitude can be influenced by interactions with discontinuities, which makes the physics of propagation phenomenon more complicated ([38],[39]). It turns out that not only the type of discontinuity affects Lamb wave scattering problem, but also crack orientation, size and even the crack zone, where the wave is reflected. To visualize the difference between wave reflection from two different parts of the crack, the numerical study

has been performed with the use of the FEM-based commercial program Abaqus 6.13-1. Four-node shell elements with reduced integration (S4R) were used to create the model.

The model of steel plate with dimensions of 125 × 125 cm and with a 25 cm × 1 cm crack cut through the plate thickness was performed (Figure 3). The damage was modeled by removing the particular finite elements. The numerical simulations were conducted for the relatively large-size damage to visualize the influence of the damage zone, from which wave is reflected on wavefront curvature. However, the developed algorithm discussed in the further part of the paper can be also used in the detection of smaller defects. The parameters of the model are summarized in Table 1. The five-cycle sine function with a central frequency of 100 kHz modulated by a Hann window was used as an excitation function. The concentrated time-dependent force equal to 1 N replaced the transducer actuation. Concentrated force can efficiently replace actuator modeling because of the high stiffness (115.00 N/μm) of the actuator ([36],[37]). The simplification results only in local (close to the excitation point) inaccuracies of simulation.

To investigate the influence of the mutual configuration of the wave source and damage on the amplitude-distance relationship, the excitation was applied perpendicularly in the numerical model in two different locations (Figure 3). The excitation source locations were chosen to impose reflections from different damage zones (end and middle points of the line crack). The distance between the crack and excitation source was chosen to avoid overlapping the incident and reflected wave. In the first case, the wave reflects from the crack edge (middle of the crack). In the second case, the excitation source lies on the crack longitudinal axis, so the wave reflects from the end point of the crack. The visualizations of the propagating wave in these two cases are presented in Figure 4 and Figure 5. When the wave reflects from the crack edge (Figure 4a-c), the amplitude of the reflected wavefront is comparable to the amplitude of the incident wave (Figure 4d), which spreads in the remaining part of the plate. The amplitude decreases and finally drops to zero on both sides of the wavefront (Figure 4e). When the wave is reflected from the end point of the damage (Figure 5a-c) the substantial difference between amplitudes of the incident and reflected wave is observable (Figure 5d,e). To analyze the amplitudes drop after reflection from different damage zones, two distance- amplitude curves were determined numerically and set in Figure 6. Additionally, the theoretical curve for an undamaged plate was also plotted for comparison. Despite identical model parameters, the shapes of the curves differ. The amplitude after reflection from the middle part of the damage changes according to theoretical predictions made for undamaged plate, but the amplitudes registered after reflection from the end point are notably lower.

Moreover, not only the amplitudes but also the shapes of the wavefronts are different for the considered cases. The radiuses of the reflected wavefront and incident wave were the same in the first case when the wave reflects from the middle part of the line crack, meanwhile, in the second case, the radius of a reflected wave was significantly smaller than the radius of the incident wave.

Table 1 Parameters of the FEM plate model

Numerical model parameters	
elastic modulus [GPa]	213
Possion ratio [-]	0.33
density [kg/m^3]	7780
linear bulk viscosity parameter	0.02
quadratic bulk viscosity parameter	1.2
element type	S4R
element size	1 x 1 mm^2
integration step [s]	10^{-7}
number of elements	1560000

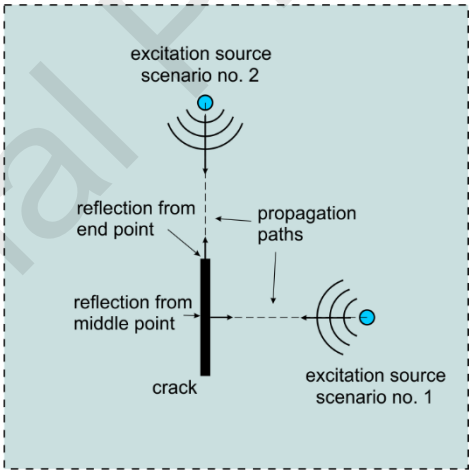

Figure 3 Numerical simulations: excitation sources locations

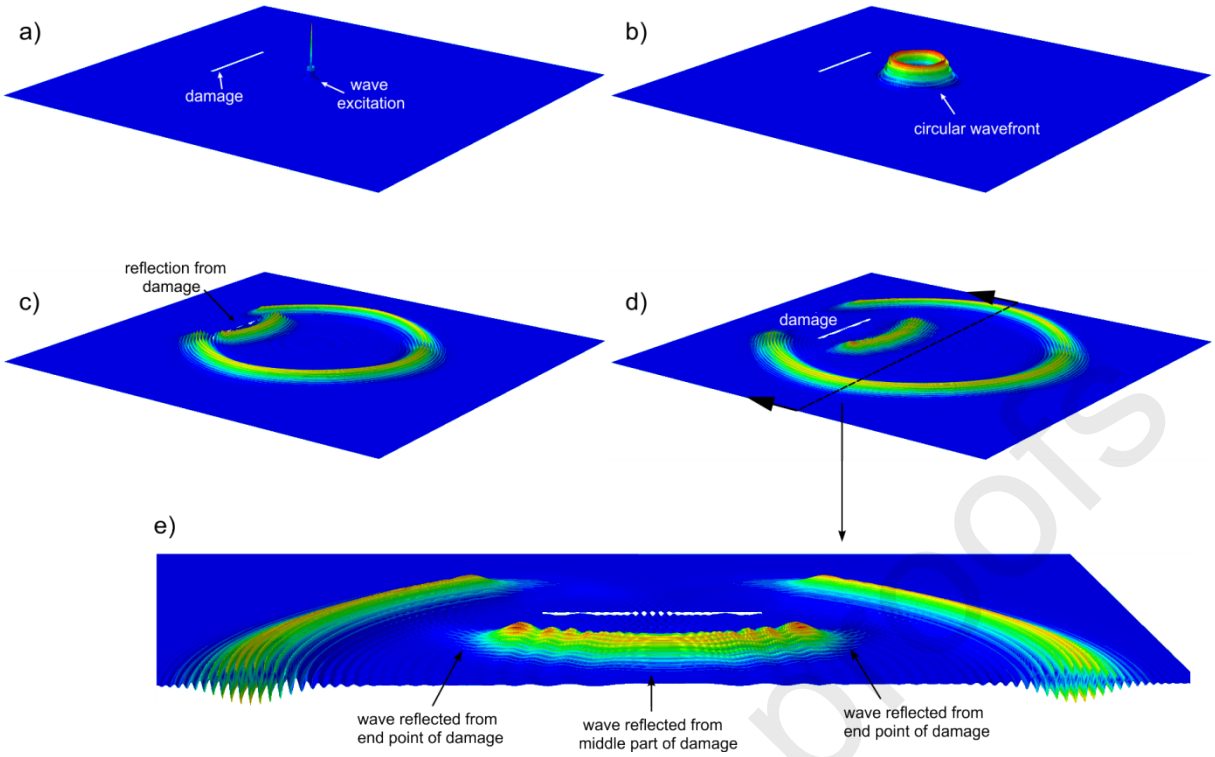

Figure 4 Numerical simulation of wave reflection from damage – scenario no. 1: a) wave excitation, b) wave propagation, c) reflection from damage edge, d) and e) propagation of reflection

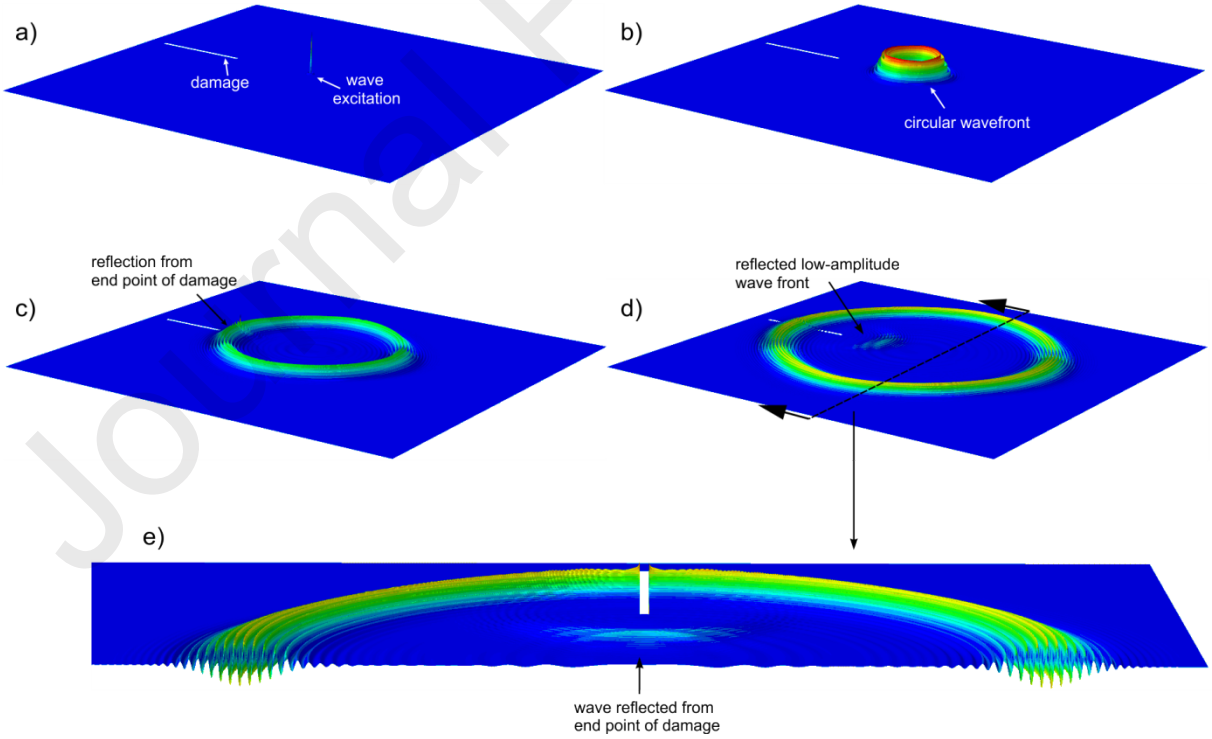

Figure 5 Numerical simulation of wave reflection from damage – scenario no. 2: a) wave excitation, b) wave propagation, c) reflection from end point, d) and e) propagation of reflection

The differences in amplitude values and wavefront shapes can be explained by the Huygens principle, which says that each point on a wavefront is a source of wavelets, which spread forward at the same speed. The new wavefront is a line tangent to all of the wavelets. When the wavefront successively reaches the line void, each point lying on its edge becomes the source of a new wave. The triggered waves interfere with each other and form a reflected wavefront. Similarly, the small-size damage (or end point of the cvoid) becomes a new wave excitation source – wave diffracts and form a new low-amplitude circular wavefront. The end point can be considered as a point wave source, while the damage edge is a line source.

The differences in both amplitudes and wavefront shapes may be efficiently utilized in diagnostics procedures developed for damage detection in metallic plates. In the next part of the paper, the algorithm of damage detection and qualification to line and small-size defects is proposed.

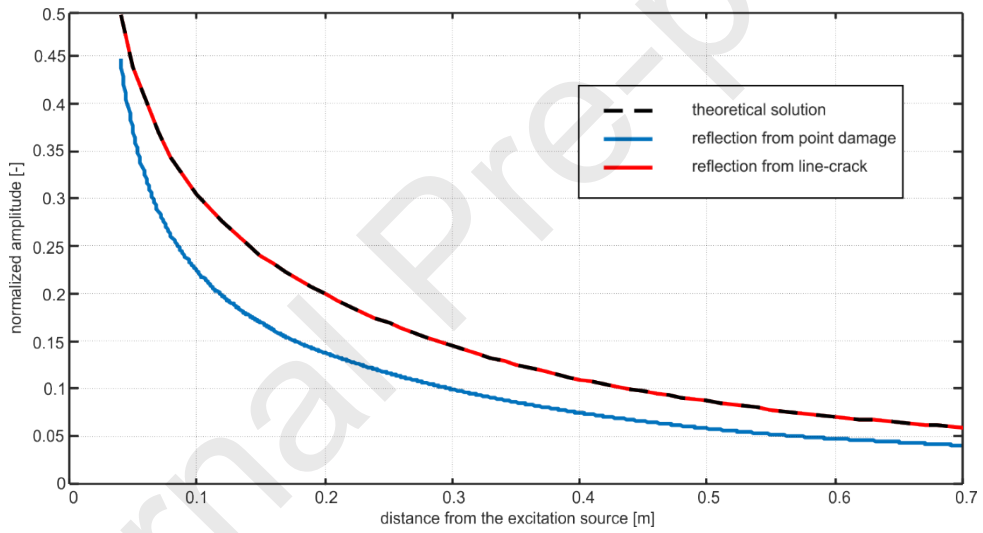

Figure 6 Numerical distance-amplitude curves determined for reflections from various damage zones compared with the theoretical solution

3. Algorithm of damage detection

3.1 Damage detection - reconstruction of the wavefront shape

Consider the sensing system with the receiver array and a single transmitter element attached at the plate with a line void. Because the plate is made of isotropic material, after excitation wave travels with the same velocity in all directions. The propagating wavefront has a circular shape and its center coincides with the actuator position. At the same time, the fictitious wave takes off from the origin denoted as A_F, which simulates the wave reflection from the damage (Figure 7a). The reflected wavefront reaches the individual sensors. Because the distances h_i between the actuator and all of n sensors are known, the average wave velocity can be determined using the times of flight of incident waves denoted as ToF^{in} registered by particular sensors:

$$v_g = \frac{1}{n}\sum_{i=1}^{n}\frac{h_i}{ToF_i^{in}}. \tag{14}$$

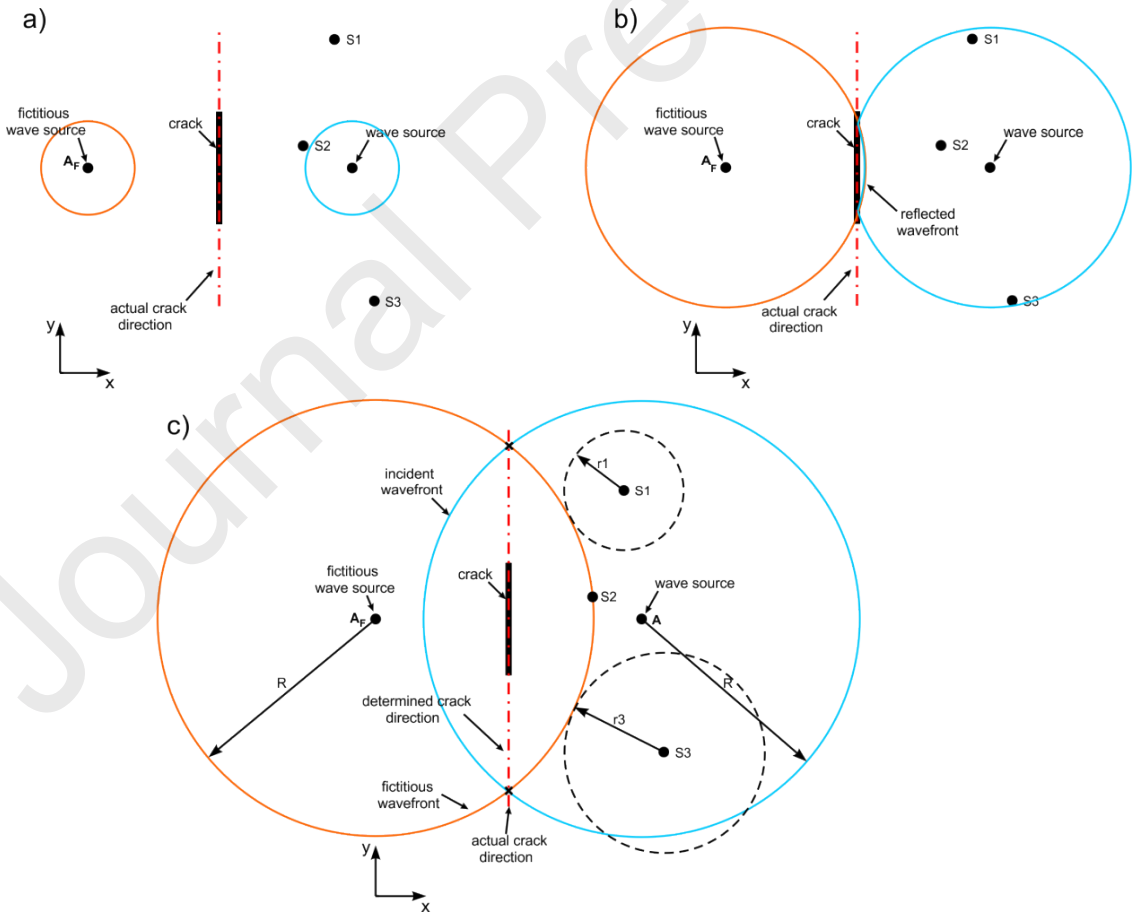

Figure 7 Scheme illustrating wave reflection from line void: a) wave excitation, b) wave reflection from damage and c) registering the reflection by the sensor S2

Determining the average wave velocity based on the incident waves registered by the sensors in the network has a very important advantage: this approach eliminates the possibility of wave packets overlapping due to i.e. reflection from plate edges.

First, the reflected wave reaches the sensor for which the propagation path is the shortest (Figure 7c). The other sensors register the reflection after Δt, which can be calculated as:

$$\Delta t_i = ToF_i^r - ToF_{\min}^r = \frac{L_i - L_{\min}}{v_g}. \tag{15}$$

where ToF_i^r is the time of flight of reflection determined for *i*-th sensor, L_i is the length of the propagation path determined for sensor *i* and $L_{\min}$ is the length of the shortest wave path. The shape of the reflected wavefront can be reconstructed based on two pieces of information:

- the reflected wavefront is tangent to circles with centers located where the sensors are placed and their radiuses are equal:

$$r_i = v_g \Delta t_i. \tag{16}$$

- the diameter of the reflected wavefront is equal to:

$$R = v_g \cdot ToF_{\min}^r. \tag{17}$$

where $ToF_{\min}^r$ is the minimal value of the time of flight determined for reflection from the defect. If the sensing system consists of at least three sensors, which are not placed in one line, it is possible to unambiguously reconstruct the wavefront shape. Moreover, the reflected wavefront is symmetrical to the originally excited incident wave, which would propagate if the plate was undamaged. The axis of symmetry of the incident and reflected wave coincides with the damage direction (Figure 7). Thus, the damage orientation can be determined if the wavefront shape is known.

3.2 Damage size estimation

The damage position and orientation can be determined by reconstructing the reflected wavefront shape but the above-described approach does not allow to estimate the damage size. In the developed method we take advantage of the difference between amplitudes of waves reflected from the middle part and end points of the damage. This stage of the algorithm requires the reference measurements to determine the distance-amplitude curve for the investigated object. The method of the curve determining and subsequent sensors rearrangement was described in Section 2.2. At least two amplitudes registered at the known distances from the excitation source must be registered to trace the curve, but increasing the number of measurements may significantly improve the quality of curve fitting.

The main idea of this part of the algorithm is based on the assumption that damage size can be unambiguously assessed if the end points of the damage are localized. To determine from which part of the damage (middle or end point) the wave was reflected, the signals must be normalized, first. Based on the known distance between actuator and *i*-th sensor h_i the theoretical amplitude value $A_i^{t,in}$ of incident waves must be calculated using the theoretical distance-amplitude curve. For each of n signals the ratio η between the theoretical and registered amplitude of incident wave must be determined:

$$\eta_i = \frac{A_i^{t,in}}{A_i^{in}}. \tag{18}$$

Then the signal $s_i(t)$ can be normalized in the following way:

$$\overline{s}_i(t) = \eta_i s_i(t). \tag{19}$$

From the normalized signals, the information (normalized amplitude $A_i^{nor,r}$ and time of flight ToF_i^r) about wave reflection from damage is extracted. The lengths of the propagation paths L_i for all of n signals are calculated as:

$$L_i = v_g \cdot ToF_i^r. \tag{20}$$

For each value of L_i the theoretical value of reflection amplitude $A_i^{t,r}$ is predicted based on the theoretical curve. In the last stage, the obtained normalized results $A_i^{nor,r}$ and theoretical predictions $A_i^{t,r}$ are compared. The ratio between the amplitudes is calculated as:

$$\delta = \frac{A^{t,r}}{A^{nor,r}}. \tag{21}$$

In the case of significant discrepancies between results (high value of δ), one can conclude that wave was reflected from the end point of the damage. If the results are consistent, the wave was reflected from the edge of the void or the plate edge. After identifying the reflection type, the size of the damage is estimated. The algorithm has been verified numerically and experimentally. The procedure of damage detection and size estimation is described step by step in the next sections.

4. Numerical verification of the algorithm

Before experimental tests, the effectiveness of the developed approach was verified numerically. In the first step the algorithm was tested based on two cases: steel plate with large-size line damage (1 cm × 25 cm) and steel plate with small-size damage (1 cm × 1cm). Next, the more complex case of a mix-mode damage was investigated. This section contains also the results of numerical simulations for damages with various lengths and widths to investigate their influence on the procedure of wavefront shape reconstruction.

4.1. Line damage detection

The parameters of the numerical model of steel plate are presented in Table 1. The transducers arrangement is presented in Figure 8. The excitation applied in point A was in the form of a modulated five-cycle sine with a central frequency of 100 kHz. The transducers were modelled using 8-nodes brick linear brick elements with reduced integration (C3D8R). Because in the real SHM application the transducers are firmly attached to the plate surface, the connection between the transducers and plate was assumed as rigid. Moreover, between sensors and the structure the adhesive layer was introduced (thickness: 1 mm, material parameters: ρ = 1400 kg/m^3, E = 1.6 GPa, ν = 0.41). The stiffness matrix of an orthotropic linear elastic material characterizing the transducers was defined based on the information obtained from the manufacturer.

The signals with their envelopes registered by the particular sensors denoted as S1-S4 in a plate with line damage are presented in Figure 9. The figure presents the results before the normalization process. According to the procedure described in Section 3, the incident waves and reflections from damage have been identified first, and they are marked with grey color. The detailed model of the transducers allowed for observing the additional reflections resulting from wave interaction with the attached sensors. Exemplary, the reflection from transducers is visible in signal registered by sensor S3 at 0.13 ms or in signal S4 at 0.3-0.4 ms. The reflections visible in the signals, which were registered later are reflections from edges of the specimen and subsequent reflections from the damage. Next, the amplitudes and the ToFs of incident and reflected waves were determined (Table 2 – columns 2-5). The ToF was considered as the peak-to-peak value. The difference between the registration time of input and output peak was calculated.

Since the distances between particular sensors are known a priori (Table 2 – columns 6), wave group velocity could be easily determined based on the ToFs (Eq. (14)) and it was equal v_g = 1736.16 m/s.

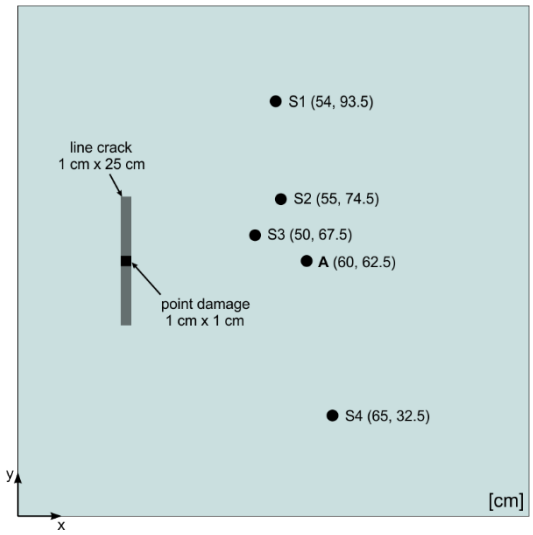

Figure 8 Numerical investigation of line damage detection: geometry of the plate and transducers arrangement

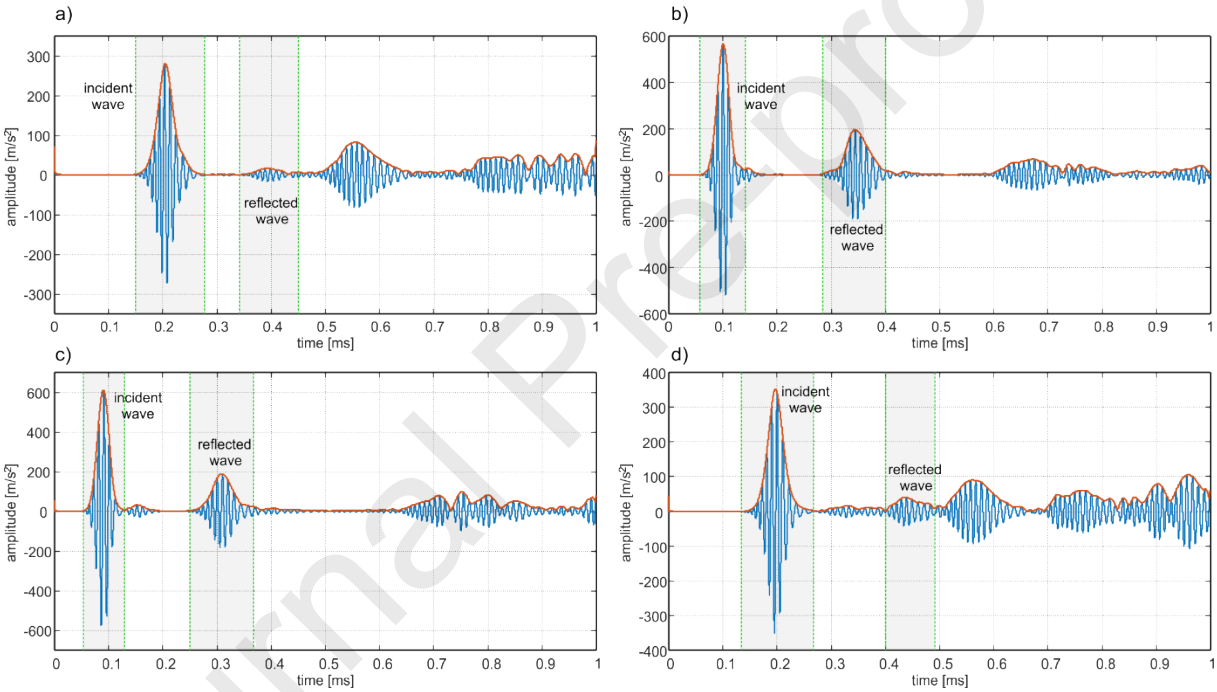

Figure 9 Numerical time-domain signals registered in node: a) S1, b) S2, c) S3 and d) S4

Table 2 Numerical results obtained for plate with line damage

sensor	time of flight [ms]		amplitude [m/s^2]		distance h sensor – actuator [cm]	theoretical amplitude of incident wave $A^{t,in}$	ratio η [$\times 10^{-4}$]
	incident wave ToF^{in}	reflected wave ToF^{r}	incident wave A^{in}	reflected wave A^{r}			
S1	0.2045	0.357	309.711	19.661	31.58	0.138	4.456
S2	0.1008	0.320	565.636	185.168	13.00	0.263	4.649
S3	0.0905	0.283	611.756	196.942	11.18	0.287	4.692
S4	0.1977	0.414	321.250	37.948	30.41	0.143	4.451

Based on the distance-amplitude curve, the theoretical amplitudes of incident waves $A^{t,in}$ were determined and the ratio η was calculated according to Eq. (18) (Table 2 – columns 7 and

8). In the next step, the signals were normalized (Eq. (19)) and the amplitudes $A^{nor,r}$ of waves reflected from damage were determined (Table 3). Based on the propagation paths lengths calculated according to Eq. (20) the theoretical amplitudes of the reflections $A^{t,r}$ were determined and then compared with the normalized amplitudes $A^{nor,r}$. The values of the ratio δ for particular signals are presented in column 5.

The high value of δ indicates high energy dissipation, which is characteristic for reflections from small-size damages or end points of the crack. For an unknown case, one would require a threshold that aided the qualification whether reflection from end or middle point was registered. In this study, the proposed threshold is equal to 1.5. If the ratio δ is higher than 1.5, one can conclude that reflection from the end point was registered. Otherwise, the wave was reflected from the middle point.

The results suggest that in this case the line-crack was detected because two different reflection types have been recognized. The amplitudes registered by sensor S2 and S3 coincide well with theoretical predictions and the δ is close to 1.0. Most probably in these sensing points, reflections from the middle part of the crack were registered. The δ for sensing points S1 and S4 is significantly higher, which indicates that the reflection energy was dissipated more intensively than theoretically predicted. One can conclude that in points S1 and S4 reflections from end points were captured. Because different types of reflections were recognized, we can also unambiguously state that the damage, while not e.g. the edge of the plate, has been detected. In the case of reflection from the plate edge, the energy dissipation would be insignificant and thus, all theoretical and numerical amplitudes after normalization would coincide with each other.

Table 3 Identifying the type of reflection – a numerical study of plate with line damage

sensor	propagation path length L [m]	normalized amplitude of reflected wave $A^{nor,r}$	theoretical amplitude of reflected wave $A^{t,r}$	ratio δ [-]	final conclusion
S1	0.620	0.00876	0.0573	6.540	reflection from end point
S2	0.555	0.08607	0.0775	0.900	reflection from middle point
S3	0.492	0.09240	0.0885	0.958	reflection from middle point
S4	0.720	0.01689	0.0658	3.896	reflection from end point

4.1.1. Reconstruction of the wavefront shape

Based on the collected results the damage direction is determined in the following section. According to Table 2, the reflection from damage was registered first at point S3, because for

this point the ToF_3^r is the shortest. To reconstruct the shape of the wavefront we have to calculate the differences between the particular *ToF*s and $ToF_{\min}$ and then determine the radiuses of circles, which are tangent to the reflected wavefront (see Eq. (16) and Table 4).

Table 4 Calculation of radiuses of the circles tangent to the reflected wavefront – line damage detection

sensor	$ToF^r - ToF^r_{\min}$ [ms]	r [cm]
S1	0.0738	12.814
S2	0.0366	6.354
S3	0.0000	0.000
S4	0.1312	22.778

The diameter of the reflected wavefront according to Eq. (17) is equal to:

$$R = v_g t_{\min} = 1736.6 \times 0.2833 \cdot 10^{-3} = 0.4919\ [m]. \tag{22}$$

To find the center of the circular wavefront with radius *R* tangent to circles with radiuses *r* and centers corresponding to the coordinates of the sensing points S1-S4 (Figure 8), the coordinates (x_F,y_F) were found, for which the minimum value of the auxiliary parameter γ_L described by the following expression was obtained:

$$\gamma_L = \sum_{i=1} \left| \sqrt{\left(x_F - x_i\right)^2 + \left(y_F - y_i\right)^2} - (R + r_i) \right|. \tag{23}$$

where x_i,y_i are the coordinates of the *i*-th sensing point. The parameter γ_L described the sum of distances between reflected wavefront and the to circles with radiuses r_i. Theoretically, in the ideal case, the value of γ_L should be equal to zero. The coordinates (x_F,y_F) were determined by using the systematic searching approach. The coordinates of the center of fictitious wavefront A_F are x_F = 0.4 [cm] and y_F = 64.2 [cm] (Figure 10). The intersection points of fictitious and actual wavefront lie of the straight line, which is the axis of symmetry of fictitious and incident wavefront. Their coordinates can be determined by solving the following equation:

$$\left(x - x_A\right)^2 + \left(y - y_A\right)^2 = \left(x - x_F\right)^2 + \left(y - y_F\right)^2. \tag{24}$$

The axis of symmetry indicates the damage direction. Figure 10 presents the coordinates of the intersection points denoted as P_1 and P_2 as well as the determined and the actual void direction. It can be seen that the damage direction determined based on the wavefront shape reconstruction coincides well with the actual crack localization.

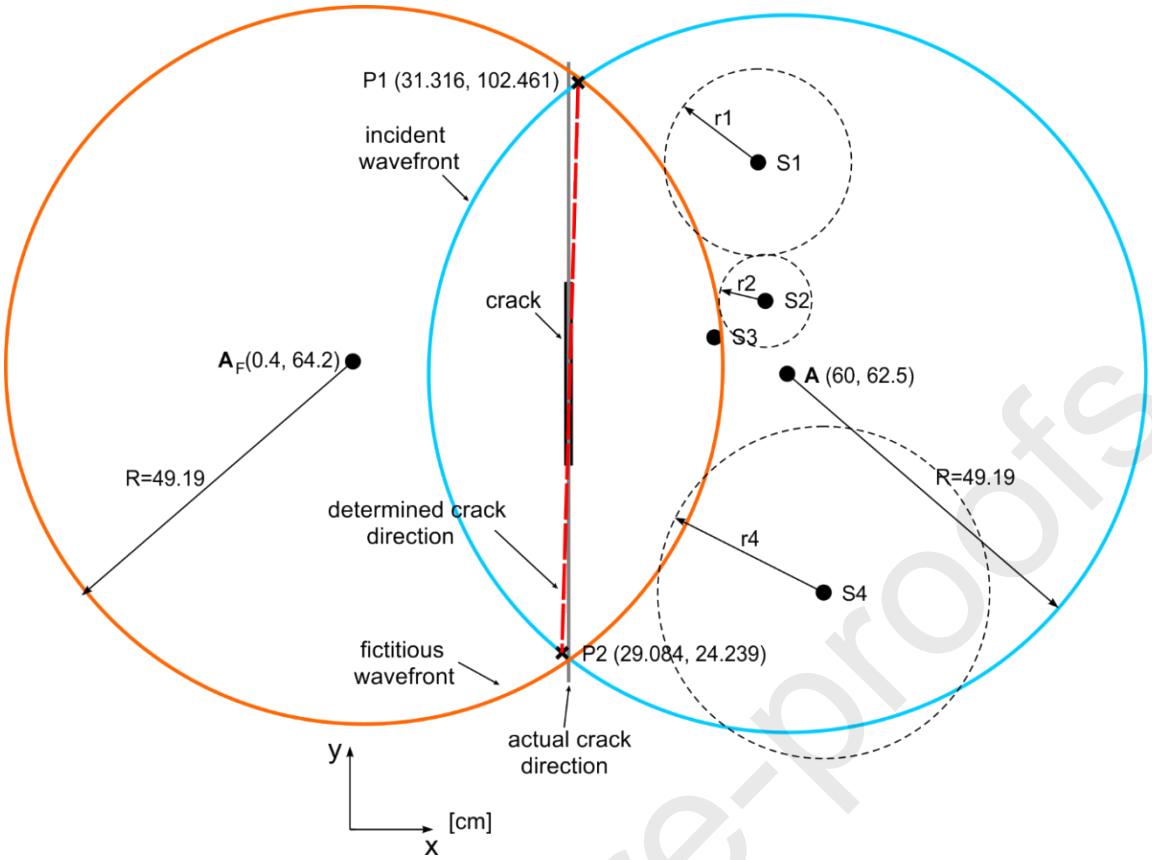

Figure 10 Determination of line-crack direction

4.1.2. Damage size estimation

To determine the exact size of the line crack, the locations of the end points must be determined. Based on the results presented in Table 3 we know that the reflections from the end points were registered in points S1 and S4. The possible location of end points can be found using the ellipse-based method. In this method, the actuation and registration points are two focal of the ellipse, while the length of the propagation path is equal to the length of the major axis. The damage lies on the circumference of the ellipse described by the equation:

$$\frac{x^2}{\left(\frac{ToF^r \cdot v_g}{2}\right)^2} + \frac{y^2}{\left(\frac{ToF^r \cdot v_g}{2}\right)^2 - \left(\frac{h}{2}\right)^2} = 1 . \tag{25}$$

Because the end points must lie of the straight line indicating the crack direction, the intersection points of line and ellipses described by Eq. (25) determined based on the signals registered in points S1 and S4 must be found. The graphical interpretation is presented in Figure 11.

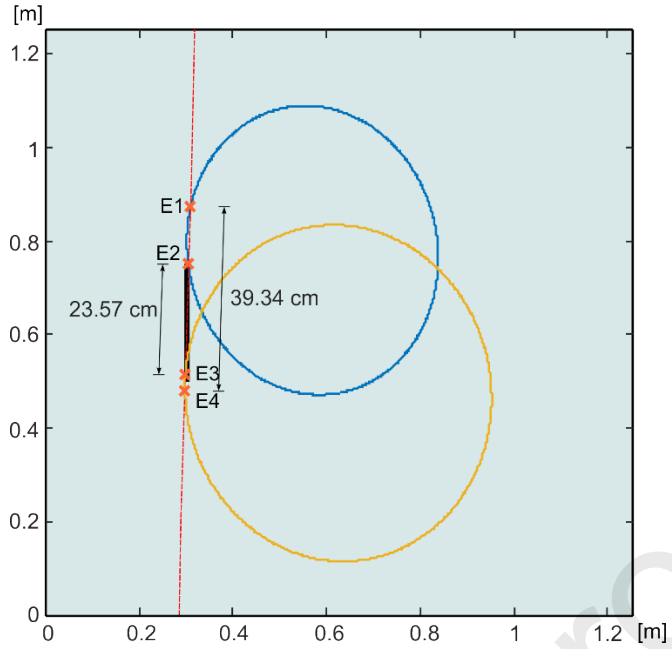

Figure 11 Determination of end points of line-crack

This example presents also the drawback of the developed approach. Four intersection points were found and each of them may the end point of the crack. The crack length is 23.57 to 39.34 cm. It can be seen that the intersection points E2 and E3 coincide with the crack ends. The distance between them corresponds to the actual damage length (25 cm). To determine the crack size unambiguously the configuration of the transducer must be rearranged or the sensors network must be extended. Despite the inaccuracy described above, the crack direction was correctly determined and its size was estimated with high accuracy using the information extracted from a very small number of registered signals.

4.2. Small-size damage detection

In the second stage of the numerical investigation, the algorithm has been verified during small-size damage detection. The transducers arrangement was the same as in the previous case, while the damage size was 1 cm × 1 cm (see Figure 8). Because the distances h between particular points, where signals were registered are the same as previously, the ToFs, numerical and theoretical values of the amplitude of incident waves are also the same. Although some of the results are identical to results obtained for line crack, they are presented here as a formality (Table 5). The changes in damage size caused the differences in the propagation path length L and in consequence in the ToF^r and the amplitudes A^r. Table 6 contains the normalized amplitudes of reflected waves and the ratios δ. In each case, the value δ is much higher than 1.0, which suggests that the theoretically predicted amplitude is higher than registered in the

signal. The high value δ indicates high energy dissipation, which is characteristic of reflections from the end points or small-size damages.

Table 5 Numerical results obtained for plate with small-size damage

sensor	time of flight [ms]		amplitude [m/s^2]		distance h sensor – actuator [cm]	theoretical amplitude of incident wave $A^{t,in}$	ratio η [$\times 10^{-4}$]
	incident wave ToF^{in}	reflected wave ToF^{r}	incident wave A^{in}	reflected wave A^{r}			
S1	0.2045	0.3983	309.711	9.465	31.58	0.138	4.456
S2	0.1008	0.3298	565.636	29.526	13.00	0.263	4.649
S3	0.0905	0.2851	611.756	45.754	11.18	0.287	4.692
S4	0.1977	0.4353	321.250	13.109	30.41	0.143	4.451

Table 6 Identifying the type of reflection – numerical study of plate with small-size damage

sensor	propagation path length L [m]	normalized amplitude of reflected wave $A^{nor,r}$	theoretical amplitude of reflected wave $A^{t,r}$	ratio δ [-]	final conclusion
S1	0.692	0.00421	0.0410	9.721	reflection from end point
S2	0.573	0.01373	0.0748	5.450	reflection from end point
S3	0.495	0.02147	0.0879	4.095	reflection from end point
S4	0.756	0.00583	0.0601	10.300	reflection from end point

Table 7 Calculation of radiuses of the circles tangent to the reflected wavefront – small-size damage detection

sensor	$ToF^{r} - ToF^{r}_{\min}$ [ms]	r [cm]
S1	0.1132	19.653
S2	0.0447	7.760
S3	0.0000	0.000
S4	0.1502	26.077

In this case, in all signals, the low-amplitude reflections were registered, which suggests that small-size damage or end point was detected. The damage direction cannot be determined using the collected data, because any reflection from the middle part of the damage was identified. The standard procedure of small-size damage localization involves the ellipse-based method however, the developed approach based on reconstruction of wavefront shape can be also efficiently used in this case.

The procedure of small-size damage detection is more difficult because the radius of the reflected wavefront is not known a priori (Figure 12a). So there are three unknowns: two

coordinates describing the location of the damage, which is a fictitious wave source (x_F,y_F) and the radius R of the reflected wavefront (Figure 12b). Based on the sketch presented in Figure 12c one can conclude that the damage coordinates x_F and y_F and wavefront radius R must satisfy the following equations:

$$\begin{cases} (x_F - x_1)^2 + (y_F - y_1)^2 = (R + r_1)^2 \\ (x_F - x_2)^2 + (y_F - y_2)^2 = (R + r_2)^2 \\ \dots \\ (x_F - x_n)^2 + (y_F - y_n)^2 = (R + r_n)^2 \end{cases}. \tag{26}$$

where n is the number of sensors in the network or the number of registration points. The radiuses r_i are presented in Table 7. The unknowns can be calculated by searching for the minimum value of the parameter γ_P which is described as follows:

$$\gamma_P = \sum_{i=1} \left| (x_F - x_i)^2 + (y_F - y_i)^2 - (R + r_i)^2 \right|. \tag{27}$$

The minimum value of γ_P was obtained for x_F = 27.95 cm, y_F = 63.06 cm and R=21.95 cm. The actual coordinates of the damage are x = 29.5 cm and y = 63 cm. The graphical interpretation of the results obtained is presented in Figure 13. The agreement of the determined location with the actual one confirms the efficiency of the method based on wavefront shape reconstruction in small-size damages detection and localization. Moreover, the novel method allows for identifying the type of detected damage based on the type of registered reflections. In such a case, we also need to take into account that the detected small-size damage may be in fact the end-point of the horizontal line crack.

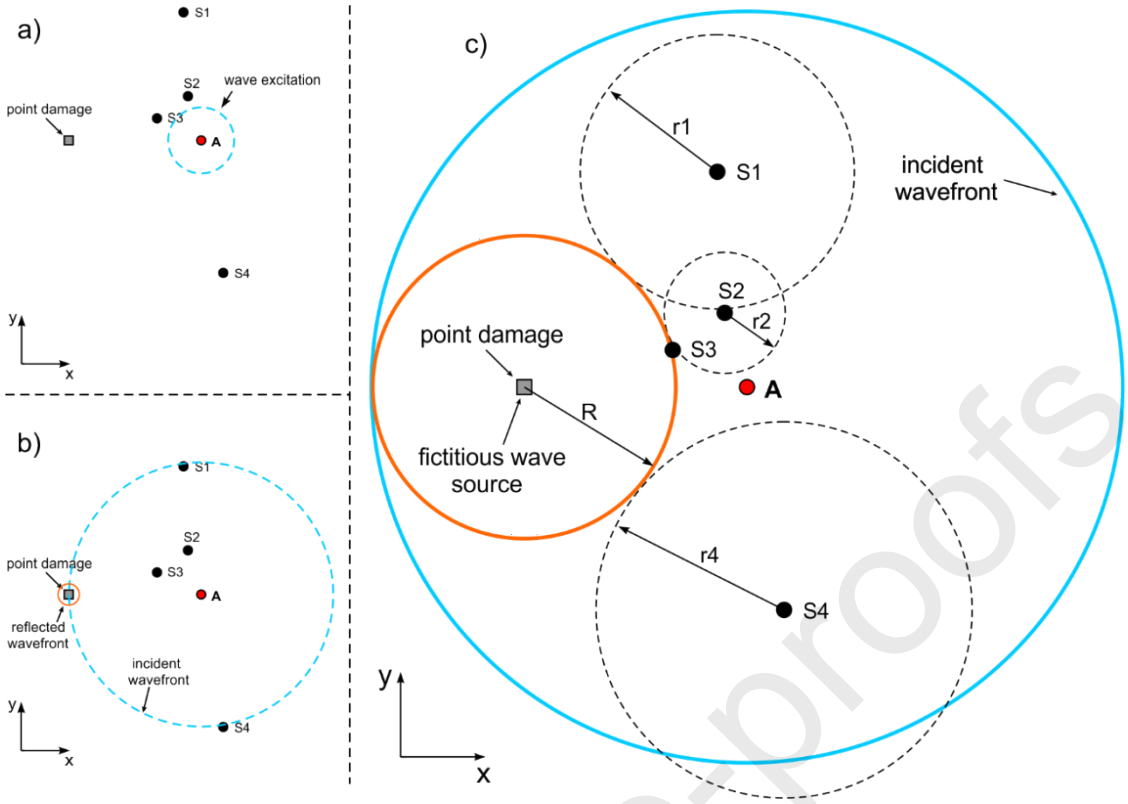

Figure 12 Small-size damage detection based on the wavefront reconstruction: a) wave excitation, b) excitation of reflected wavefront and c) registration of reflected wavefront by the sensor S3

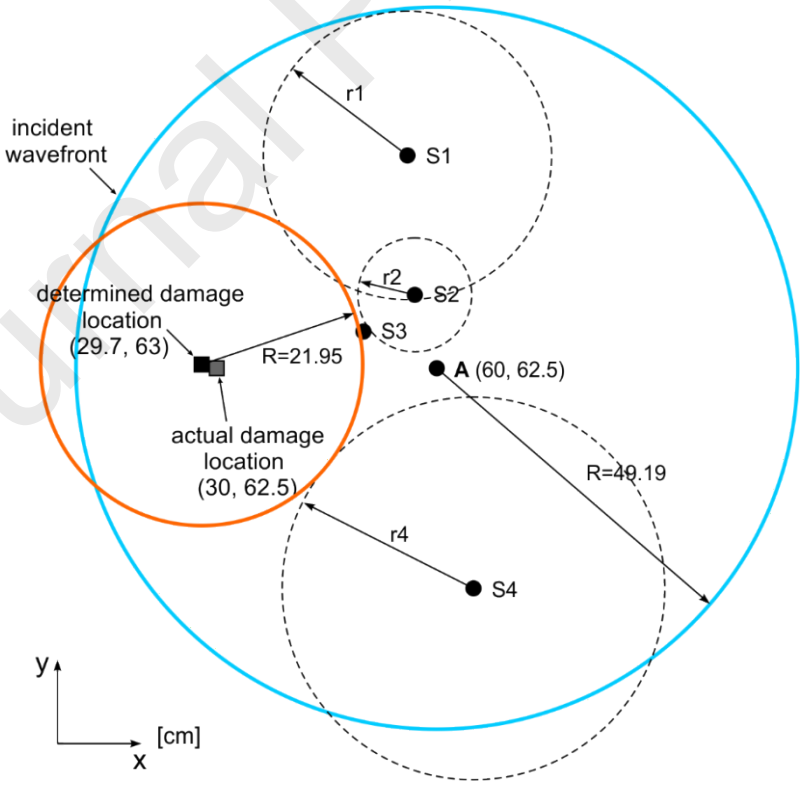

Figure 13 Wave reflection from the small-size damage – graphical interpretation of numerical results

4.3. Mix-mode crack detection

In real cases, the damage is usually characterized by irregular shape which can additionally affect the wave propagation signals. Therefore, the numerical simulations have been also performed for more complex case of the common damage type: mix-mode crack (Figure 14a). In this case, the crack was modelled as a lack of connection between finite elements, so its width is equal to 0 cm. Because the crack is not linear, the reflected wavefront is not perfectly circular which is the basic assumption of the proposed approach (compare Figure 14b and Figure 4d). The results obtained after signal processing are summarized in Table 8 and Table 9. Because the reflection registered by sensor S3 has been classified as a reflection from the middle point of the damage, the direction of the crack as well as its size has been determined using the procedure for line cracks (section 4.1). The final result of damage detection and size estimation is presented in Figure 15. The length of the crack has been overestimated (14.13 cm instead of 10 cm) and the exact direction could not be exactly determined, however the inaccuracies are not significant despite the more complex shape of the crack.

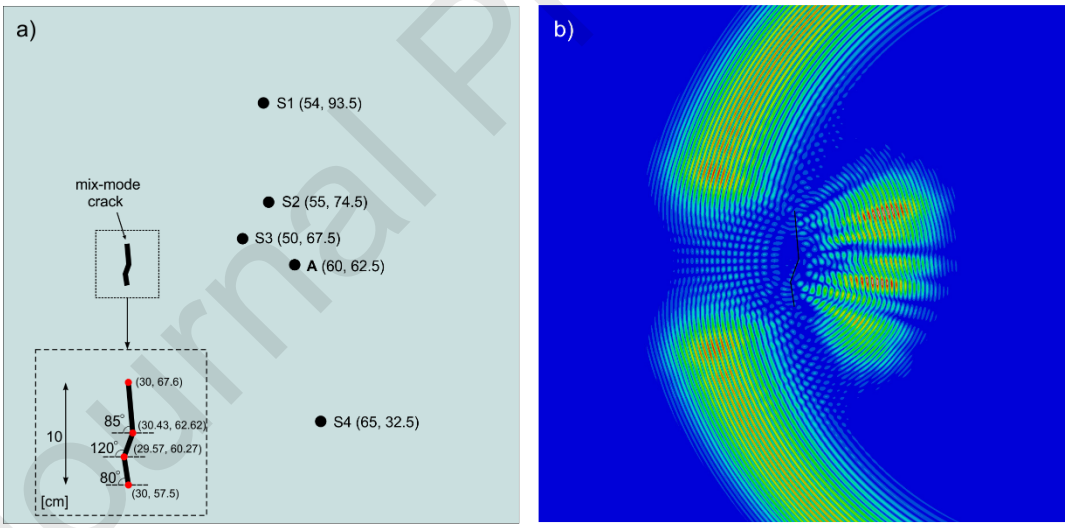

Figure 14 Wave reflection from the mix-mode crack – graphical interpretation of numerical results

Table 8 Numerical results obtained for plate with mix-mode crack

sensor	reflected wave: amplitude [m/s²]	reflected wave: time of flight ToF^r [ms]	propagation path length L [m]	normalized amplitude of reflected wave $A^{nor,r}$	theoretical amplitude of reflected wave $A^{t,r}$	ratio δ [-]	final conclusion
S1	7.510	0.365	0.634	0.00342	0.0666	19.473	end point
S2	91.019	0.315	0.547	0.04231	0.0788	1.862	end point

S3	143.437	0.273	0.474	0.06730	0.0921	1.368	middle point
S4	63.735	0.424	0.736	0.02836	0.0558	1.967	end point

Table 9 Calculation of radiuses of the circles tangent to the reflected wavefront – mix-mode damage detection

sensor	$ToF^r - ToF^r_{\min}$ [ms]	r [cm]
S1	0.092	15.973
S2	0.042	7.291
S3	0.000	0.000
S4	0.151	26.160

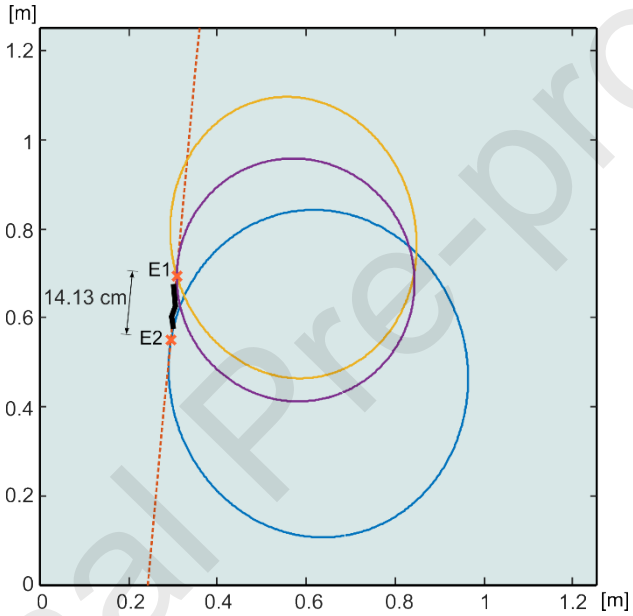

Figure 15 Wave reflection from the mix-mode crack – graphical interpretation of numerical results

4.4. The influence of sensors configuration

In this section the results of numerical simulations for various crack lengths (20, 15, 10 and 5 cm) are summarized. Moreover, to indicate the possible limitations of the algorithm, two different configurations of sensing points were investigated.

Figure 16 presents numerically simulated wave reflections from cracks with varying lengths. The configuration of sensing and excitation point was the same as in the previous cases (see Figure 8). In all cases, the amplitude and the curvature of the reflection are comparable to the amplitude and curvature of the incident wave. Therefore, one can expect that line crack will be detected in all cases. Table 10 contains the summarized results obtained for all configurations. The type of reflection registered in particular sensing points has been

recognized and the final remark whether line crack or small-size defect was detected has been formulated.

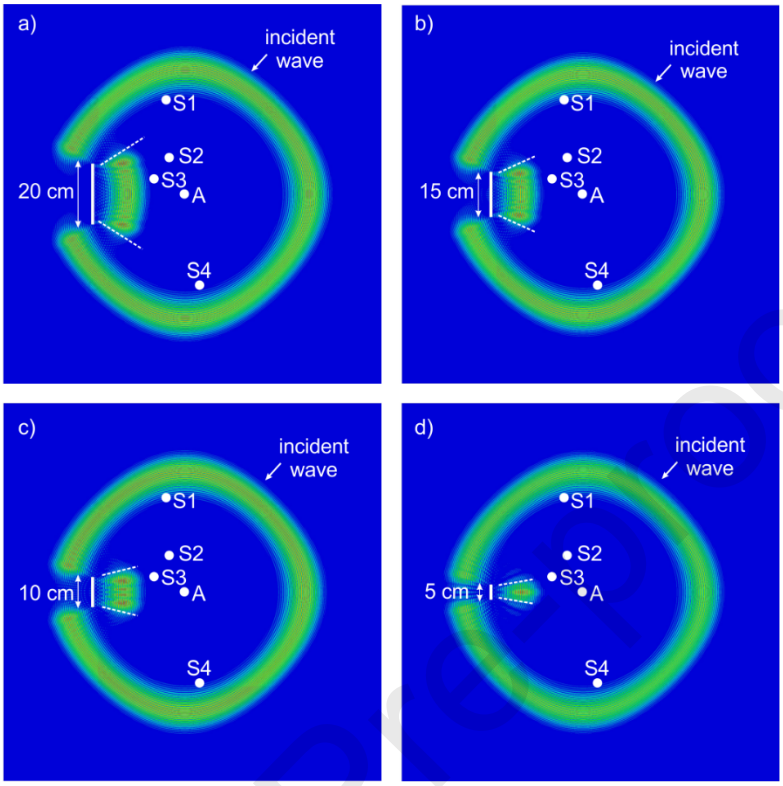

Figure 16 Numerical simulation of wave reflection form the crack with length a) 20 cm, b) 15 cm, c) 10 cm and d) 5 cm

Table 10 Results of numerical simulations: type of reflections

recogniztion of the reflections types				
sensor	crack length 20 cm	crack length 15 cm	crack length 10 cm	crack length 5 cm
S1	end point	end point	end point	end point
S2	middle point	end point	end point	end point
S3	middle point	middle point	middle point	end point
S4	end point	end point	end point	end point
final remark	line crack	line crack	line crack	small-size damage

In three cases of longer cracks (20, 15 and 10 cm), two types of reflections have been registered (reflection from end and middle point), which suggests that the line crack has been detected. In the case of a crack with a length of 5 cm only reflections from the end point have been registered, which means that the procedure of small-size defect detection presented in Section 4.2 would be applied to determine the position of the small-size damage. Following this procedure would lead to erroneous results, because in fact, the detected damage is not small-size damage but line crack. The incorrect recognition of damage type is not the result of the

incorrect algorithm developed in the previous sections, but the unfavorable configuration of sensing and excitation points. To prove this the results for crack with a length of 5 cm were collected again, but this time different configurations of sensing points have been used. The position of the excitation point remained unchanged, but the distances in the vertical direction between excitation and sensing points have been reduced 4 times. For the rearranged configuration two types of reflections have been recognized (Table 11), which means that in such a case the procedure for line crack detection would be used. In Figure 17 the graphical explanation of the difference between the results obtained for various configurations is presented. For both configurations, the shortest propagation paths excitation damage-sensing point were determined.

Table 11 Type of reflections for rearranged configuration and crack length of 5 cm

sensor	recognition of the reflections types
S1	end point
S2	middle point
S3	middle point
S4	end point
final remark	line crack detected

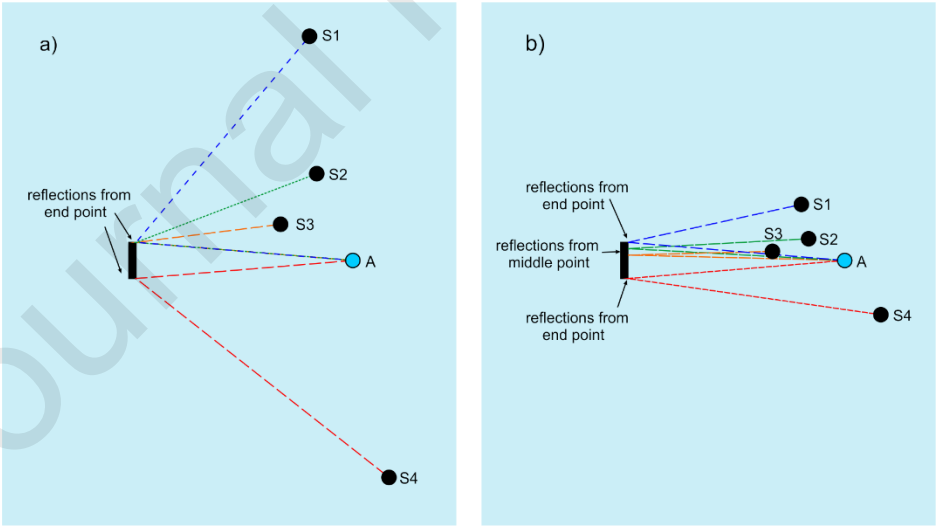

Figure 17 The shortest propagation paths for various configurations of sensing and excitation points: a) initial configuration, b) rearranged configuration with reduced distances between excitation and sensing points in vertical direction

As we can see the initial configuration presented in Figure 17a did not allow for registering the reflection from the middle point and in consequence did not allow for detection of the line crack and estimation of its size. After configuration rearrangement reflections from

middle points were registered in numerical signals and the proper recognition of the damage type was possible.

The results presented indicate that the method can be used also in the detection of smaller cracks, however the classification of damage type depends not only on correct ToF estimation or proper determination of distance-amplitude curve but also on sensors configuration.

4.5. The influence of damage width

The cases presented in the previous section concern the line defects with constant width equal to 1 cm. In the following section, the results of numerical simulations for plates with damages characterized by different widths are presented. Two extreme cases were investigated: the first case concerns the plate with a notch with a length of 10 cm. The damage was modelled as a lack of connection between the finite elements and there is no gap between notch boundaries. The second extreme case is the rectangular large-scale damage characterized by the same width and length. The shape of the reflected wavefront is identical in both cases. The main difference visible in snapshots is the presence of the low-amplitude wave diffracted at the end points of the notch (Figure 18a).

In both cases, the amplitude of the incident waves remained the same but the amplitudes of reflections from the defect slightly differed. Table 12 contains the values of the particular amplitudes and the classification of reflection type. Despite the differences in amplitudes resulting from propagation and interference of diffracted wave, as well as the reflections from the transducers, in both cases after signal processing, the same reflection types have been recognized.

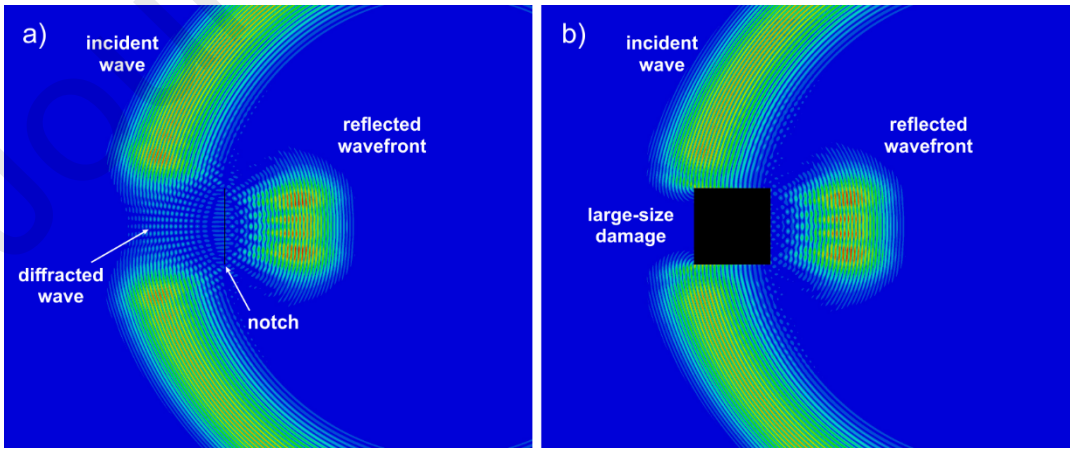

Figure 18 Reflection from damage with a width of a) 0 cm and b) 10 cm

Table 12 Comparison of the amplitudes and classification of the reflection types

	notch (width 0 cm)		large-scale damage (width 10 cm)	
sensor	amplitude	reflection type	amplitude	reflection type
S1	6.79	end point	7.14	end point
S2	31.69	end point	33.26	end point
S3	154.41	middle point	161.7	middle point
S4	3.66	end point	4.41	end point
final remark		line crack detected		line crack detected

The width of damage did not affect the time of flight and therefore the determined direction of the detected defect is the same in both cases (Figure 19). The wave is reflected from the right, vertical edge of the crack, and thus only the size and the direction of this edge can be determined. If we want to determine the width of other defect dimensions the sensor networks must be enriched and rearranged (Figure 19).

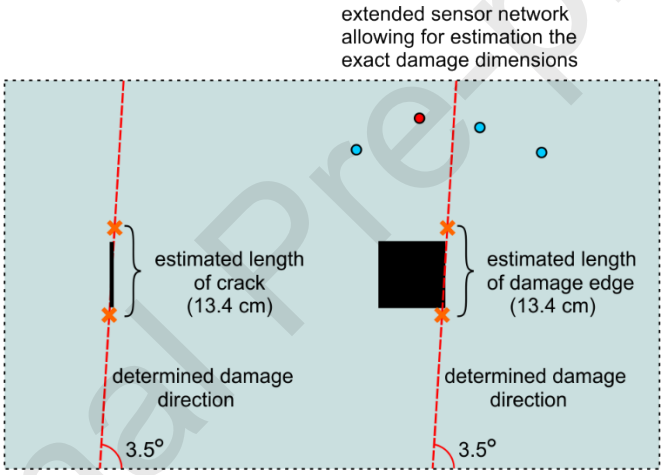

Figure 19 Reflection from damage with a width

5. Experimental investigation

5.1. Experimental model

Experimental tests were conducted on metallic plate made of steel S235 (E = 213 GPa, ν= 0.33, ρ = 7780 kg/m^3) with dimensions 0.1 cm × 125 cm × 125 cm. The damage in the form of void was cut through the plate thickness. The dimensions of the damage were 1 cm x 25 cm. The geometry of the experimental model is presented in Figure 20.

The guided waves were excited and registered with the use of multilayer piezo transducers Noliac NAC2012 with dimensions 3 mm × 3 mm × 2 mm. attached at the plate surface by wax. The input voltage was 10 V. The measurements were carried out with the device PAQ-1600D. The sampling frequency was 2 MHz (Nyquist frequency 1MHz). The system manufactured by EC Systems has built-in filters; the output signal was limited by a second-order lowpass filter with a cutoff frequency of 525kH, while the input signal was filtered by a set of two filters: a highpass filter with a cutoff frequency of 2kHz and a lowpass filter with a cutoff frequency of 750kHz.

The usual excitation signal in the form of the windowed tone burst was used in Lamb wave inspection. The five-cycle sinusoidal signal with a central frequency of 100 kHz was modulated with the Hann window to reduce the dispersion effect. Central frequency was chosen based on the results of the tuning test. Because the presented study is devoted to considering the novel method, the readability of signal and ease of interpretation were of particular priority. The initial tuning test involved the excitation and registration of several time-domain signals with various excitation frequencies. In the next step, the signals were compared. The analysis included the comparison of the signal amplitude, spreading the wave packets caused by dispersion effects and signal readability. The frequency for which the high-quality, readable signals were registered was chosen.

The average experimental wave velocity of antisymmetric mode was equal to 1836.7 m/s. The distance-amplitude curve for the considered experimental plate model has been presented in Figure 2. The procedure of curve determining has been described in Section 2.3.

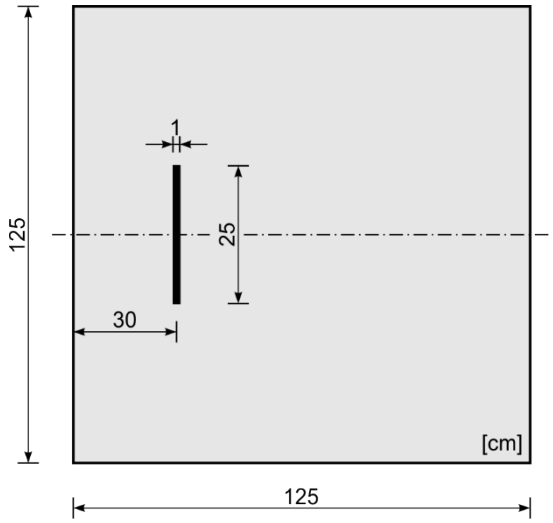

Figure 20 Geometry of the experimental model

5.2. Transducers configurations

The experimental tests were conducted for four different transducers configurations. The locations of piezo elements in configurations I, III and IV were chosen very freely, while the configuration II was designed by reducing the number of sensors used in configuration I. The use of a variable number of sensors allows for the assessment of the effectiveness of the developed method for various numbers and positions of piezo transducers. The most extensive sensor network consisted of six transducers, while the less extensive – three. It is noteworthy that three transducers so far was the minimal number to unambiguously determine the position of the small-size damage. Using the wavefront shape reconstruction method, not only the crack damage can be detected, but also its size can be estimated with the data collected from only three signals.

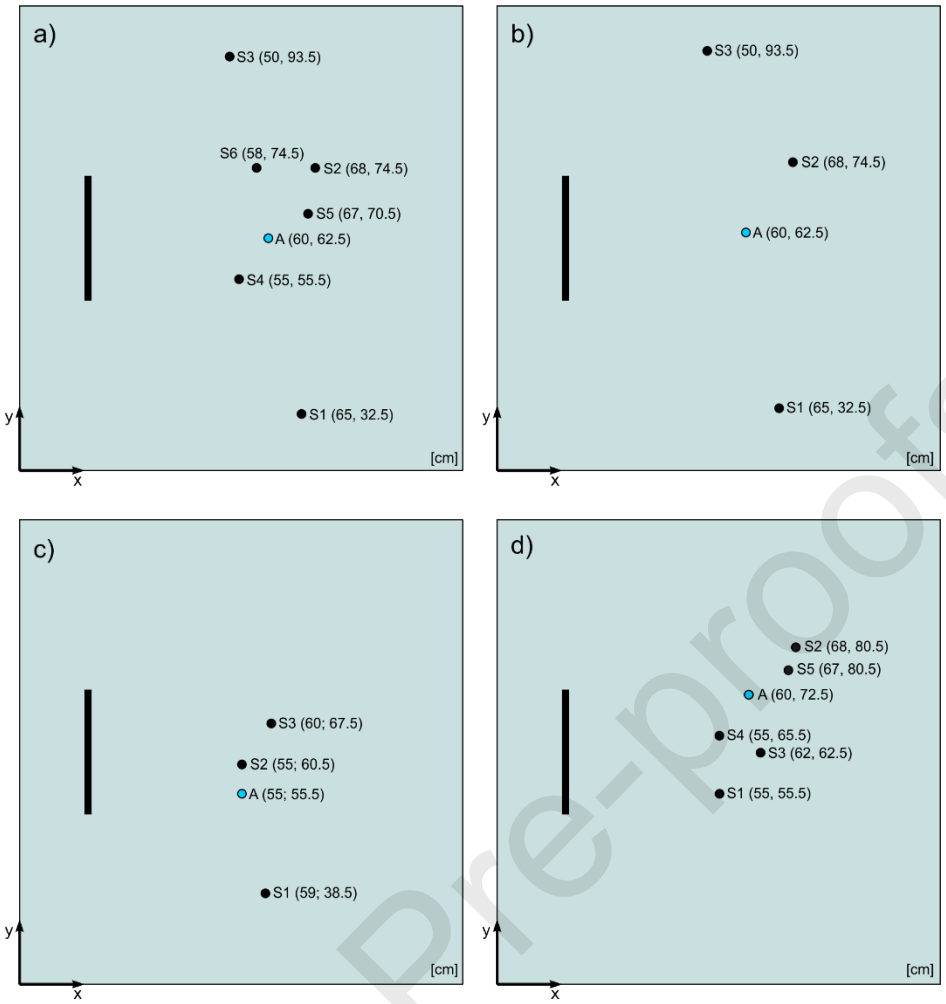

Figure 21 Configurations of piezo transducers: a) configuration I, b) configuration II, c) configuration III and d) configuration IV

The presentation of the results for several different configurations would also allow to indicates the possible difficulties and drawbacks of the novel approach. The results presented in this section show that it is practically always possible to determine the crack direction based on the shape of the reflected wavefront, however, the possibility of estimating the crack size strongly depends on the configuration of the transducers and is independent of the method's effectiveness.

5.3. Experimental results

5.3.1 Configuration I

The experimental time-domain signals registered by the sensors S1-S6 included in configuration I are presented in Figure 22. The incident waves and reflections from damage were identified and distinguished with the grey color. As mentioned in section 2.2 according to dispersion relation for frequency of 100 kHz only one antisymmetric mode A0 and one

symmetric mode S0 can be excited. Because of imperfect transducers attachment, mode conversion and geometric imperfections, usually two fundamental modes differing in amplitudes are observed in experimental signals [40]. This is also the case here: the low-amplitude symmetric modes have been identified and marked in obtained signals. It propagates after incident A0 mode and its excitation may the result of the mode conversion. The other peaks registered in signals later are the result of wave reflections from boundaries. Next, the signals were processes and the important data were extracted and summarized in Table 13.

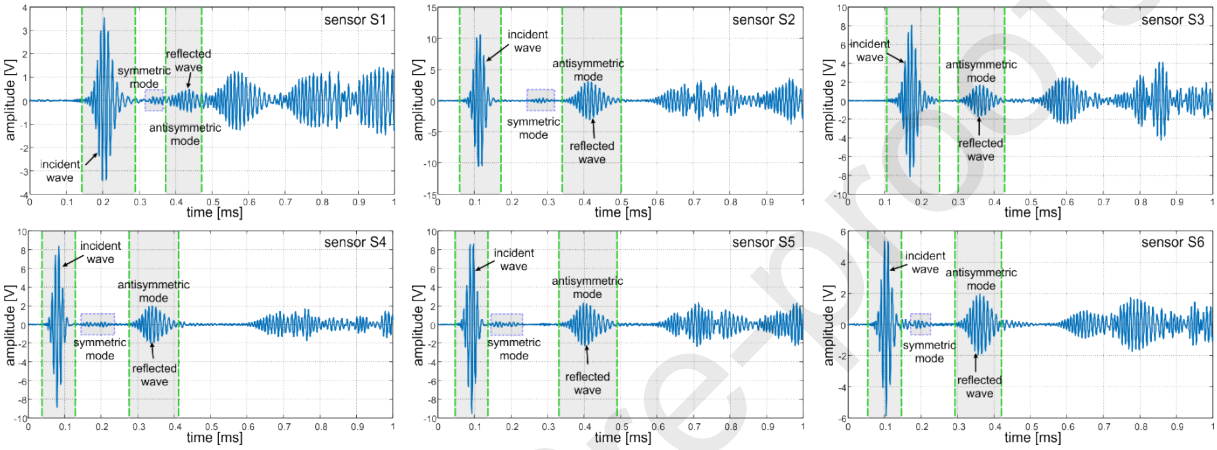

Figure 22 Time-domain signals registered for the configuration I

Table 13 Damage detection in steel plate – results for configuration I

sensor	time of flight reflected wave ToF^r [ms]	propagation path length L [m]	normalized amplitude of reflected wave $A^{nor,r}$	theoretical amplitude of reflected wave $A^{t,r}$	ratio δ [-]	final conclusion
S1	0.374	0.687	0.0199	0.0606	3.045	reflection from end point
S2	0.347	0.637	0.0622	0.0662	1.000	reflection from middle point
S3	0.297	0.545	0.0288	0.0791	2.747	reflection from end point
S4	0.276	0.507	0.0748	0.0857	1.146	reflection from middle point
S5	0.335	0.615	0.0713	0.0690	0.968	reflection from middle point
S6	0.295	0.542	0.0888	0.0796	0.896	reflection from middle point

Two sensors (S1 and S3) registered the reflection with a relatively low amplitude ($\delta > 1.5$). In the rest of the cases, the reflection amplitude was close to the value determined theoretically ($\delta < 1.5$). The results suggest that two different types of reflections were registered, which means that line crack damage has been detected. Moreover, because two different sensors captured reflections from two different end points, crack size can be also estimated in this case. The results of the wavefront shape reconstruction obtained using Eqs. (22)-(24) are presented in Table 14 and Figure 23. The radius of the incident wave R was 50.693

cm and the coordinates of the center of fictitious wavefront A_F in centimeters were (4.9, 63.7). The determined damage direction is correct, but the shift of both axes indicating the actual and determined damage direction possibly results from the accuracy of the estimation of the time of flight and the wave velocity.

Table 14 Calculation of radiuses of the circles tangent to the reflected wavefront – configuration I

sensor	$ToF^r - ToF^r_{\min}$ [ms]	r [cm]
S1	0.098	18.000
S2	0.071	13.041
S3	0.021	3.857
S4	0.000	0.000
S5	0.059	10.837
S6	0.019	3.490

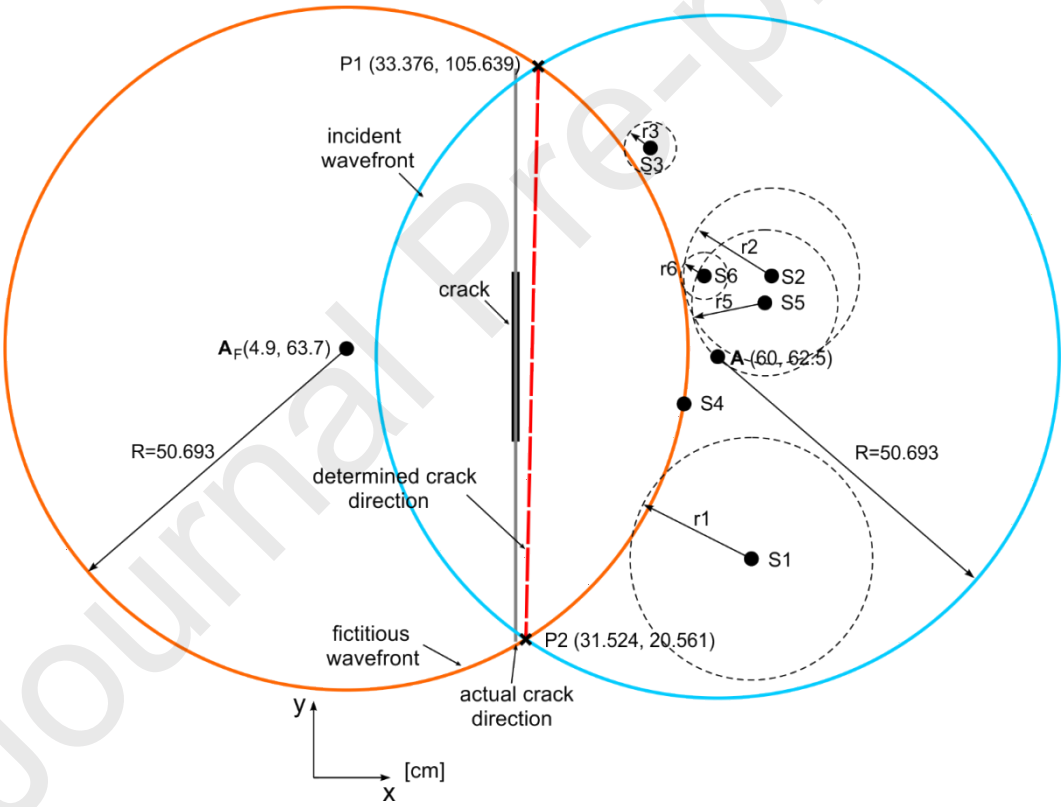

Figure 23 Determination of crack orientation – configuration I

In the next step, the ellipse-based method was used to localize the end-points of the crack. The ellipses were plotted for sensors S1 and S3 and presented in Figure 24. There were four intersection points. The crack size estimated based on the presented results is equal from 22 to 43.3 cm. The actual crack length is within the specified range. The results for the other sensors configurations were processed in the same way and they are presented and discussed in the further sections.

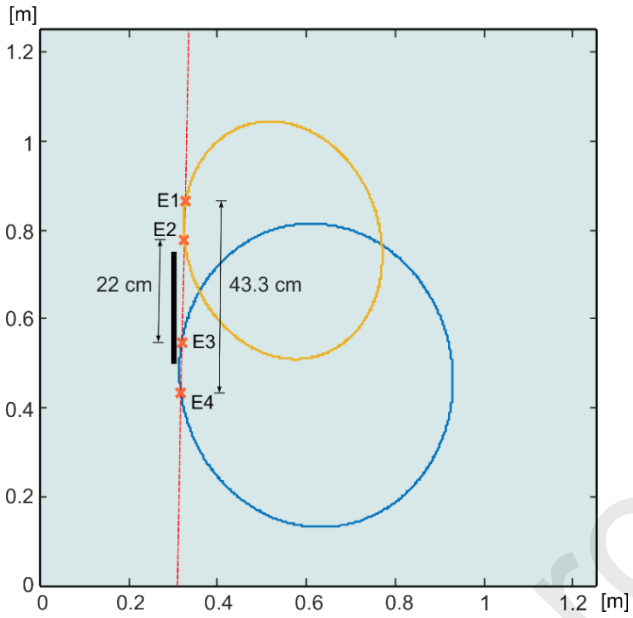

Figure 24 Determination of crack size – configuration I

5.3.2 Configuration II

As mentioned, the configuration II was created by removing the sensors S4, S5 and S6 from configuration I. Despite the less extensive sensor network, two different types of reflections were identified also in this case. At least two reflections from different end points allow to estimate the crack size (Table 15). The reconstructed wavefront based on tangent circles (

Table 16) and the determined crack direction is presented in Figure 25, while the final result is shown in Figure 26.

Table 15 Damage detection in steel plate – results for configuration II

sensor	time of flight reflected wave ToF^r [ms]	propagation path length L [m]	normalized amplitude of reflected wave $A^{nor,r}$	theoretical amplitude of reflected wave $A^{t,r}$	ratio δ [-]	final conclusion
S1	0.374	0.687	0.0199	0.0606	3.045	reflection from end point
S2	0.347	0.637	0.0622	0.0662	1.000	reflection from middle point
S3	0.297	0.545	0.0288	0.0791	2.747	reflection from end point

Table 16 Calculation of radiuses of the circles tangent to the reflected wavefront – configuration II

sensor	$ToF^r - ToF^r_{\min}$ [ms]	r [cm]
S1	0.077	14.142
S2	0.050	9.184

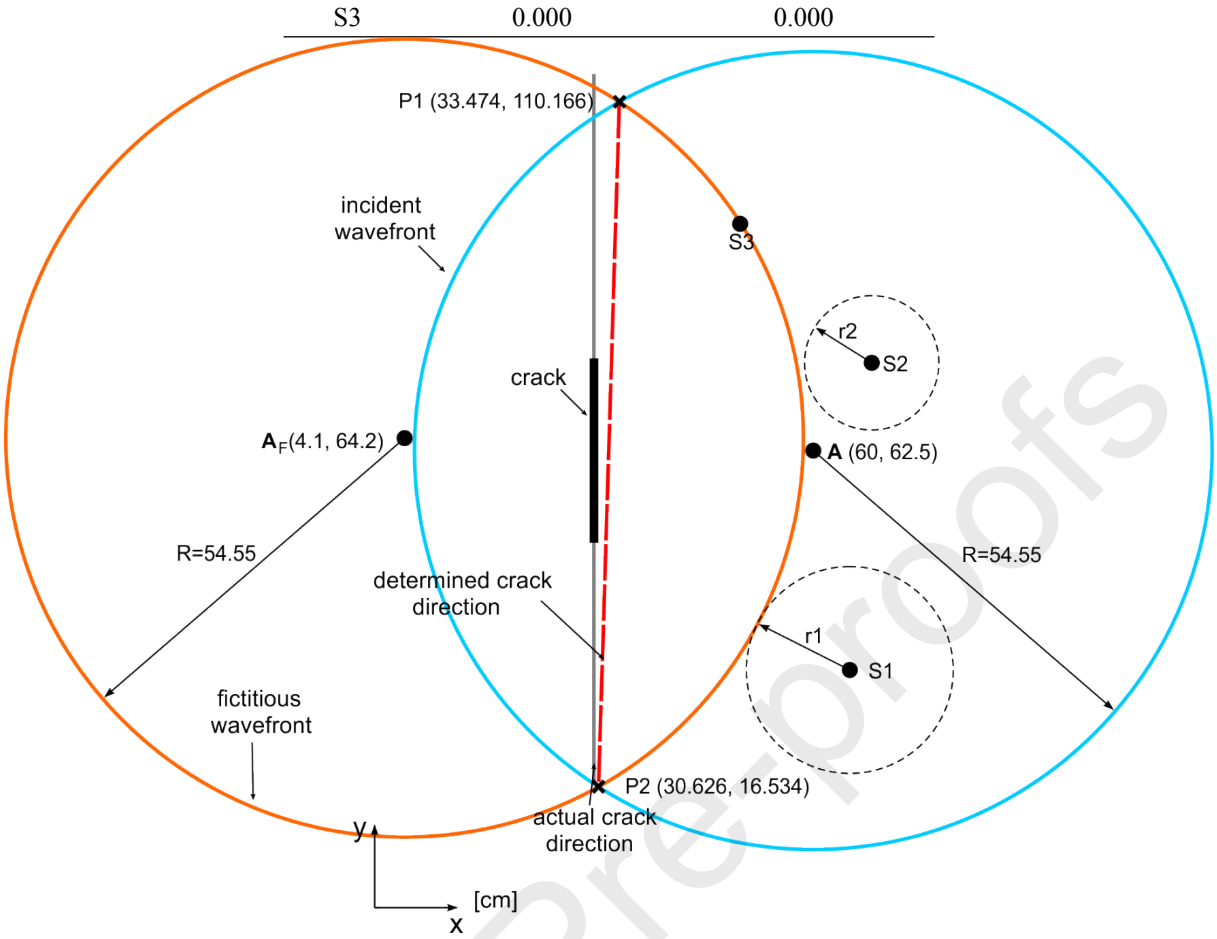

Figure 25 Determination of crack orientation – configuration II

The estimated damage is equal from 29.29 cm to 35.72 cm. The reduction of the number of the sensor did not degrade the quality of the results, but even improved it. The length of the damage was identified with greater accuracy than for configuration I. Moreover, it has been shown that both detection and size estimation of the damage is possible with just three signals. Limiting the number of sensors results in a reduction in the amount of processed data, shortening the analysis time and thus reducing the costs related to monitoring, which is the most important advantage of the proposed method.

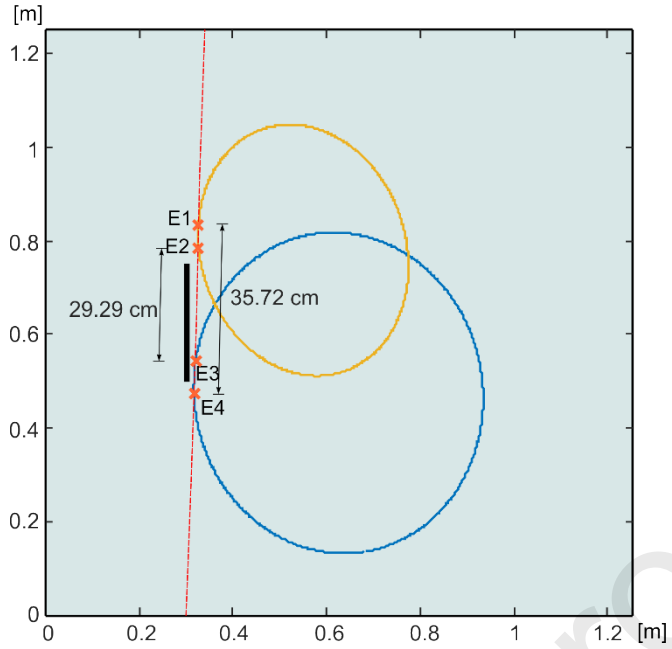

Figure 26 Determination of crack size – configuration II

5.3.3 Configuration III

Configurations III and IV were designed so that to present the possible difficulties and the drawbacks of the described method.

The data presented in Table 17 and Table 18 were processed in the same way as in the previous cases. Even though two different types of reflections have been registered, which indicates the development of line crack damage, only one sensor (S1) registered the reflection from the crack end point.

Table 17 Damage detection in steel plate – results for configuration III

sensor	time of flight reflected wave ToF^r [ms]	propagation path length L [m]	normalized amplitude of reflected wave $A^{nor,r}$	theoretical amplitude of reflected wave $A^{t,r}$	ratio δ [-]	final conclusion
S1	0.293	0.538	0.0174	0.0802	4.609	reflection from end point
S2	0.247	0.454	0.0725	0.0964	1.330	reflection from middle point
S3	0.290	0.533	0.0780	0.0810	1.038	reflection from middle point

Table 18 Calculation of radiuses of the circles tangent to the reflected wavefront – configuration III

sensor	$ToF^r - ToF^r_{\min}$ [ms]	r [cm]
S1	0.046	8.449
S2	0.000	0.000
S3	0.043	7.898

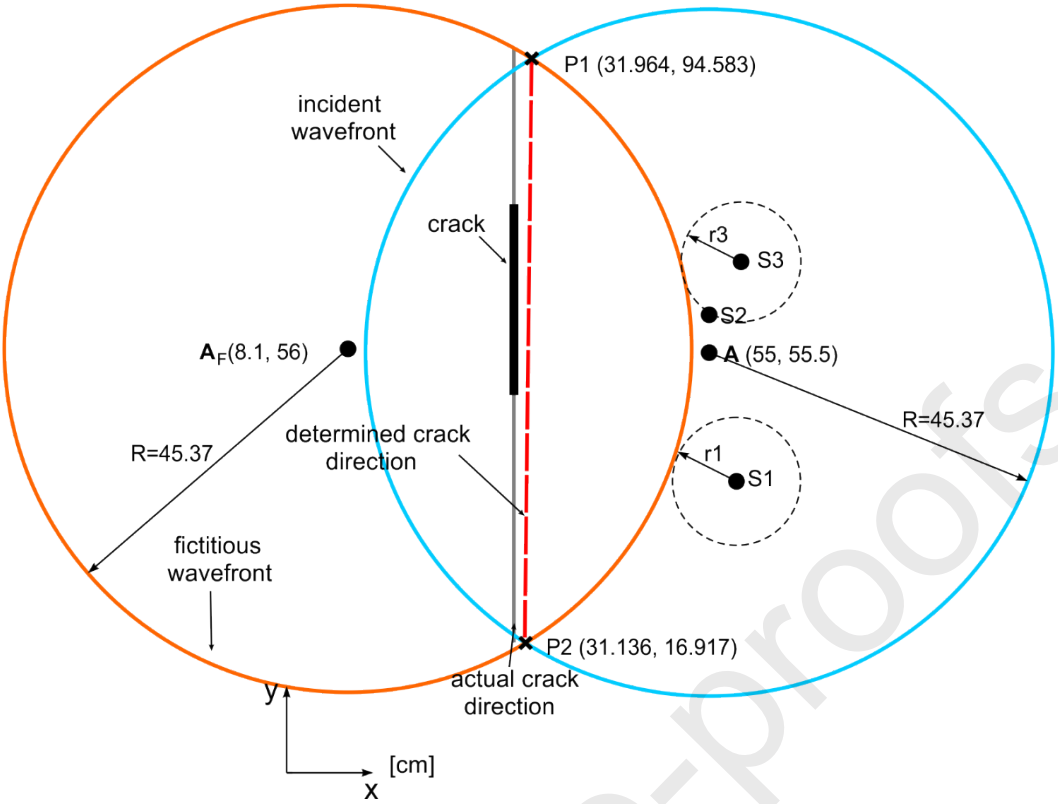

Figure 27 Determination of crack orientation – configuration III

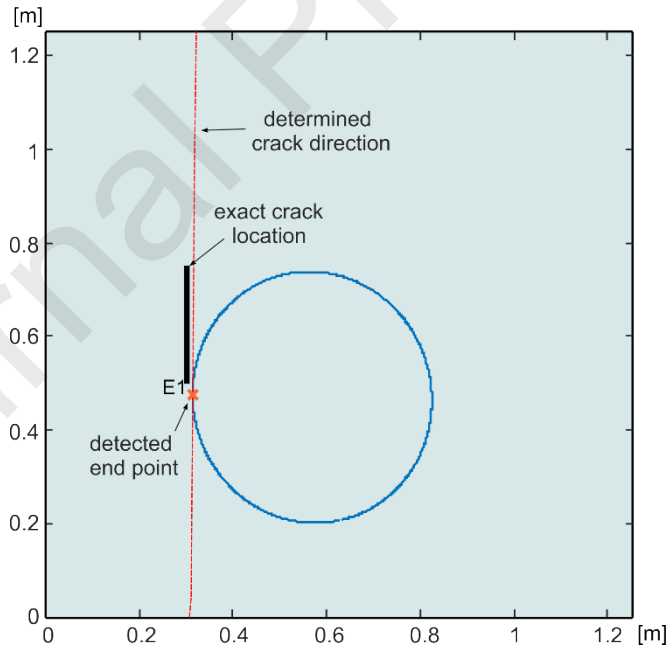

Figure 28 Determination of crack size – configuration III

Results obtained for the third transducers configuration allow for the determination of the crack direction, but its unambiguous size estimation is not possible in this case. In the figure, the determined location of the one of end points has been presented. Its location coincides with the location of the actual crack end-point. This kind of situation requires the redesigning of the

sensor network. Based on the recommendations presented in the paper [24] which proves that the more scattered the sensors are, the longer crack can be efficiently detected, the most advantageous would be the relocation of the sensor S3.

5.3.4 Configuration IV

The results for the last configuration are presented in Table 19 and Table 20. The values of the ratio δ vary from 0.834 to 1.037 which means that all sensors registered reflections from the middle part of the crack.

Table 19 Damage detection in steel plate – results for configuration IV

sensor	time of flight reflected wave ToF^r [ms]	propagation path length L [m]	normalized amplitude of reflected wave $A^{nor,r}$	theoretical amplitude of reflected wave $A^{t,r}$	ratio δ [-]	final conclusion
S1	0.314	0.577	0.0852	0.0741	0.870	reflection from middle point
S3	0.342	0.628	0.0807	0.0673	0.834	reflection from middle point
S4	0.302	0.555	0.0748	0.0776	1.037	reflection from middle point

Table 20 Calculation of radiuses of the circles tangent to the reflected wavefront – configuration IV

sensor	$ToF^r - ToF^r_{\min}$ [ms]	r [cm]
S1	0.012	2.204
S2	0.040	7.349
S3	0.000	0.000

Based on the reconstructed wavefront the direction of the crack has been determined with very high accuracy (Figure 29). Unfortunately, since any sensor registered the reflection from the end point, the crack size cannot be estimated.

In general, for each sensors configuration, there exists a certain limit length of the crack, which can be detected. The detectable limit length depends only on the position of the extreme transducers. Based on the formulae derived in the paper [24] the detectable limit length of the crack for configuration IV was calculated and it is equal to 5.47 cm. The actual crack length is significantly longer, which means that the inability to estimate the crack size results from the inadequate transducers configuration, but not from the deficiencies in the developed method. In such a case the configuration must be re-designed. The most advantageous would be to scatter the sensors along the axis that indicates the crack direction, which would highly increase the detectable crack length.

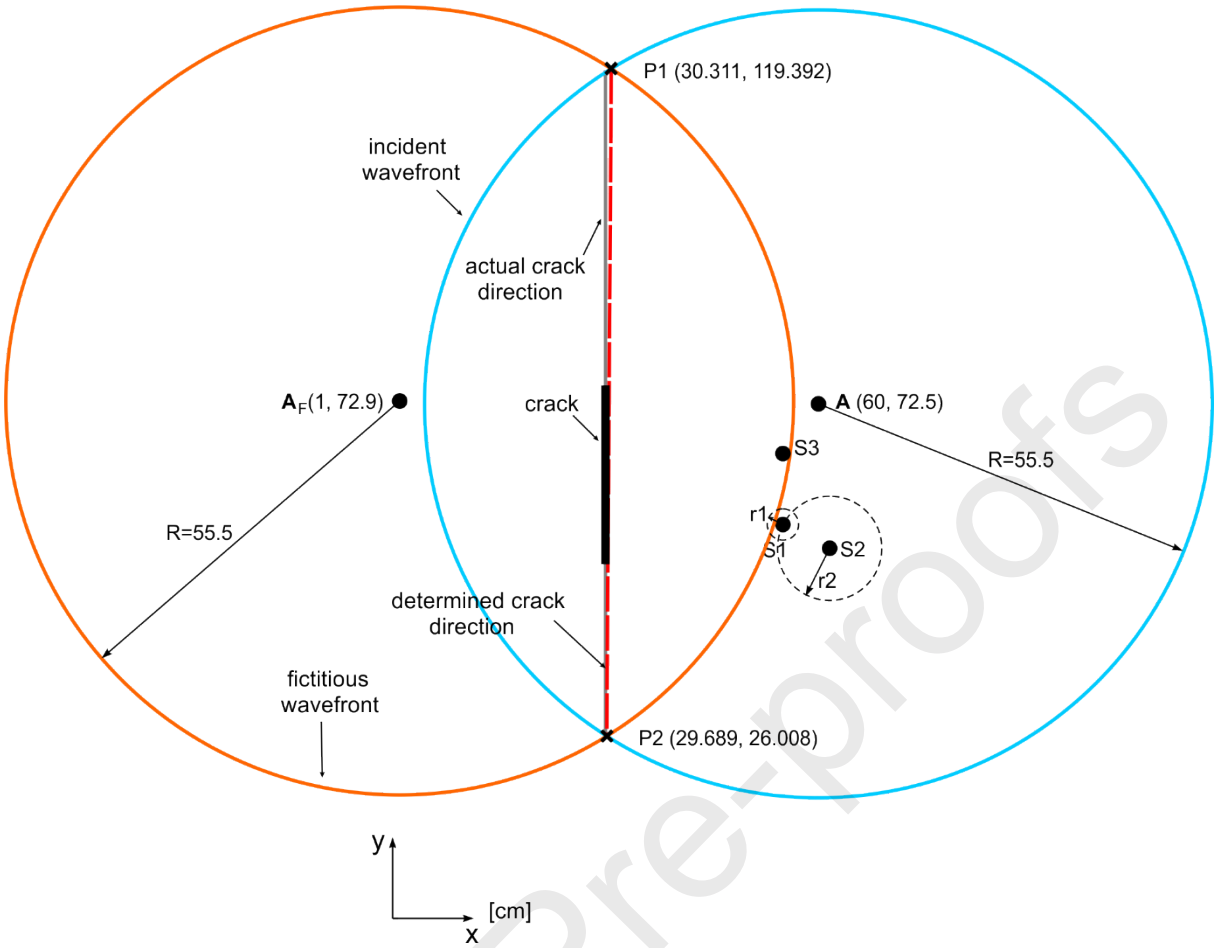

Figure 29 Determination of crack orientation – configuration IV

6 Discussion and future work

The results presented in the previous section indicated that the developed algorithm based on wavefront curvature reconstruction can be used in damage detection in plate-like structures. Despite some important advantages like high effectiveness and a very small number of necessary sensors, the presented approach has also some limitations, which must be considered in the future study. First of all, the damage size considered in the paper is rather big. The line crack was 25 cm long. The significant crack size allowed for clear observation of the relationship between wavefront shape and damage orientation. The algorithm can be also effectively used in the detection of shorter line cracks and small-size damages.

The procedure of damage detection based on wavefront reconstruction requires some baseline measurement to determine the shape of the distance-amplitude curve. The curve can be exactly determined based on the significant number of experimental measurements of the amplitudes registered at different distances from the source, or the number of measurements can be smaller, but the knowledge about the material parameters is then essential to trace the dispersion curve. The dispersion curves can be determined experimentally with the use of one of the common methods [41], but still, some baseline information of measurement is required. Moreover, the considered plate was characterized by relatively simple geometry. In real cases, the presence of rivets, stiffeners, irregular edges may affect wave propagation signals. However, it should be noted that in this study the method without the need for the collection of reference measurement by PZT network for undamaged structure was proposed. However, the proposed method can be used for constant monitoring of the damage development. The sensor network installed permanently on the structure may be part of the SHM system – in such a case the reflections from stiffeners or rivets can be easily identified because they are registered at the same time and are characterized by the same amplitude. Moreover, the location of the additional elements (stiffeners, rivets, edges) usually can be also determined based on the project of the structure (or the project of the element of the structure).

The presented study did not take into account the inaccuracies resulting from the ToF estimation. Meanwhile, the inaccuracy in the ToF estimation may lead to inaccuracy in the location of the damage. Even though the deviations in the ToF should not negatively affect the recognition of the type of reflection (reflection from the end or middle point), but it may influence on the determined angle of inclination of the crack (see Figure 25). As mentioned in Section 4.1 the ToF was considered here as the peak-to-peak value. However, there are also other approaches to the ToF calculation ([42]-[44]), which may lead to slight differences in the

determined lengths of propagation paths. Further studies should include also the formulation of the criteria allowing for the assessment of the accuracy of the damage detection.

The developed algorithm has been applied in damage detection in metallic plates. Because of material isotropy wave travels with the same velocity in every direction. The practical application of the discussed method requires the consideration of other materials. In the case of other materials i.e. laminates, the reconstruction of wavefront shape curvature can be more complicated and definitely must be considered in the future study.

7 Conclusions

This article presents the novel method of line-damage size detection and size determination based on the reconstruction of the shape of the reflected wavefront. The developed algorithm takes advantage of the differences in amplitudes and radiuses of wavefronts reflected from various parts of the damage. The diagnostic abilities of the novel method has been verified during the experimental and numerical investigation conducted for steel plates with both line crack and small-size damage. Several various configurations of the transducers were used to present the effectiveness of the developed approach, as well as its limitations. Based on the conducted study, some important conclusions can be drawn:

- The method based on wavefront reconstruction allows for recognizing the type of detected damage. Based on the normalized amplitude of the reflected wave one can recognize whether point damage or line crack was detected.
- Crack orientation and size can be efficiently estimated with the use of only three sensors, which so far was the minimal number to detect small-size damage. Minimizing the number of the sensors shortens the analysis time and in a further perspective reduces the cost of the monitoring system.
- The transducers configuration strongly influences the results of the damage detection. The damage orientation can be determined if the sensors network consists of at least three sensors, which are not placed in one line, but the damage size estimation requires a properly designed configuration of sensors. In general, the more scattered the sensors, the longer crack can be detected.

References

[1] J.L. Rose, Ultrasonic guided waves in structural health monitoring, Key. Eng. Mat. 270-273 (2004) 14-21.

[2] Su, Z. et al, Guided Lamb waves for identification of damage in composite structures: a review, J. Sound. Vib. 295 (2006) 753-780.

[3] A.Raghavan, CES. Cesnik, Review of guided wave structural health monitoring, Shock. Vib. Digest, 39(2) (2007) 91-114.

[4] M. Mitra, S. Gopalakrishnan, Guided wave based structural health monitoring: a review, Smart. Mat. Struct. 25(5) (2016) 27.

[5] N.P. Yelve, M. Mitra, P. Mujumdar, Detection of delamination in composite laminates using lamb wave based nonlinear method. Compos. Struct. 159 (2017) 257–266.

[6] B. Yang, F.Z. Xuan, Y. Xiang, D. Li, W. Zhu, X. Tang, Lamb wave-based structural health monitoring on composite bolted joints under tensile load, Materials 10(6) (2017) 652.

[7] Y. Ren, L. Qiu, S. Yuan, F. Fang, Gaussian mixture model-based path-synthesis accumulation imaging of guided wave for damage monitoring of aircraft composite structures under temperature variation, Struct. Health. Monit. 18(1) (2019) 284-302.

[8] S. Shoja, V. Berbyuk, A. Boström, Guided wave-based approach for ice detection on wind turbine blades, Wind. Eng. 42(5) (2018) 483-495.

[9] B. Zima B, M. Rucka, Non-destructive inspection of ground anchors using guided wave propagation, Int. J. Rock Mech. Min. 94 (2017) 90-102.

[10] Z. Hanfei, C. Shuhao, M. Shiwei, L. Yu, X. Hanyu, X. Qingwei, L. Yanyan, Z. Haiyan, Multi-sensor network for industrial metal plate structure monitoring via time reversal ultrasonic guided wave, Measurement, 152 (2020) 107345.

[11] H. Cho, M. Hasanian, S. Shan, C.J. Lissenden, Nonlinear guided wave technique for localized damage detection in plates with surface-bonded sensors to receive Lamb waves generated by shear-horizontal wave mixing, NDT&E Int. 102 (2019) 35-46.

[12] P.S. Tua, S.T. Quek, Q. Wang, Detection of crack in plates using piezo-actuated Lamb waves, Smart. Mat. Struct. 13 (2004) 643–660.

[13] T. Wandowski, P. Malinowski, W. Ostachowicz, Damage detection with concentrated configurations of piezoelectric transducers, Smart. Mat. Struct. 20 (2011) 025002.

[14] M. Radzieński, Ł. Doliński, M. Krawczuk, M. Palacz, Damage localization in a stiffened plate structure using a propagating wave, Mech. Sys. Signal. Pr. 39 (2013) 388-395.

[15] C. Xu, Z. Yang, Z. Zhai, B. Qiao, S. Tian, X. Chen, A weighted sparse reconstruction-based ultrasonic guided wave anomaly imaging method for composite laminates. Compos. Struct. 209 (2019) 233-241.

[16] H. Zhang, J. Hua, F. Gao, J. Lin, Efficient Lamb-wave based damage imaging using multiple sparse Bayesian learning in composite laminates, NDT&E Int. 116 (2020) 102277.

[17] M. Bahador, A. Zaimbashi, R. Rahgozar, Three-stage Lamb-wave-based damage localization algorithm in plate-like structures for structural health monitoring applications, Signal. Pr. 168 (2020) 107360.

[18] N. Mori, S. Biwa, T. Kusaka, Damage localization method for plates based on the time reversal of the mode-converted Lamb waves, Ultrasonics 91 (2019) 19-29.

[19] S. Zhang, C. Li, W. Ye, Damage localization in plate-like structures using time-varying feature and one-dimensional convolutional neutral network, Mech. Sys. Signal. Pr. 147 (2021) 107107.

[20] H. Zuo, Z. Yang, C. Xu, S. Tian, X. Chen, Damage identification for plate-like structures using ultrasonic guided wave based on improved MUSIC method. Compos. Struct. 203 (2018) 164-171.

[21] L. Huang, L. Zeng, J. Lin, N. Zhang, Baseline-free damage detection in composite plates using edge-reflected Lamb waves. Mech. Sys. Signal. Pr. 247 (2020) 112423.

[22] Z. Wang, P. Qiao, B. Shi, Application of soft-thresholding on the decomposed Lamb wave signals for damage detection of plate-like structures. Measurement 88 (2016) 417-427.

[23] Z. Liu, K. Sun, G. Song, C. He, B. Wu, Damage localization in aluminum plate with compact rectangular phased piezoelectric transducer array. Mech. Sys. Signal. Pr. 70-71 (2016) 625-636.

[24] B. Zima, M. Rucka: Guided waves for monitoring of plate structures with linear cracks of variable length: Arch. Civ. Mech. Eng. 16(3) (2016) 387-396.

[25] J. Hua, F. Gao, L. Zeng, J. Lin, Modified sparse reconstruction imaging of lamb waves for damage quantitative evaluation: NDT and E Int. 107 (2019) 102143.

[26] H. Zhang, J. Hua, F. Gao, J. Lin, Efficient Lamb-wave based damage imaging using multiple sparse Bayesian learning in composite laminates: NDT and E Int. 116 (2020) 102277.

[27] R. Kazys, L. Mazeika, R. Barauskas, R. Raisutis, V. Cicenas, A. Demcenko, 3D analysis of interaction of Lamb waves with defects in loaded steel plates,Ultrasonics 44 (2006) 1127–1130.

[28] H. Duflo, B. Morvan, J.L. Izbicki, Interaction of Lamb waves on bonded composite plates with defects, Compos. Struct. 79 (2007) 229–233.

[29] A. Ghadami, M. Behzad, H.R. Mirdamadi, A mode conversion-based algorithm for detecting rectangular notch parameters in plates using Lamb waves, Arch. Appl. Mech, 85 (2015) 793-804.

[30] C. Ramadas, K. Balasubramaniam, A. Hood, M. Joshi, C.V. Krishnamurthy, Modelling of attenuation of Lamb waves using Rayleigh damping: Numerical and experimental studies, Compos. Struct., 93 (2011) 2020-2025.

[31] B. Zima, R. Kędra, Detection and size estimation of crack in plate based on guided wave propagation, Mech. Syst. Signal. Pr., 142 (2020) 106788.

[32] P.D. Wilcox, A rapid signal processing technique to remove the effect of dispersion from guided wave signals, IEEE Trans. Ultrason. Ferroelectr. Freq. Control 50 (2003) 419–427.

[33] C-B. Xu, Z-B. Yang, X-F. Chen, S-H. Tian, Y Xie, A guided wave dispersion compensation method based on compressed sensing, Mech. Syst. Signal. Pr. 103 (2018) 89-104.

[34] J. L. Rose, Ultrasonic Guided Waves in Solid Media, Cambridge University Press, 2014.

[35] V. Giurgiutiu, Structural Health Monitoring with Piezoelectric Wafer Active Sensors, Academic Press, 2014.

[36] H. Gravenkamp, Efficient simulation of elastic guided waves interacting with notches, adhesive joints, delaminations and inclined edges in plate structures: Ultrasonics, 82 (2018) 101-113.

[37] A.C. Kubrusly, P. Tovar, J.P. von der Weid, S. Dixon, Mode conversion of SH guided waves with symmetry inversion in plates, Ultrasonics, 112 (2021) 106334.

[38] C. Schaal, A. Mal, Lamb wave propagation in a plate with step discontinuities, Wave Motion 66 (2016) 177-189,

[39] B. Poddar, V. Giurgiutiu, Scattering of Lamb waves from a discontinuity: an improved analytical approach, Wave Motion 65 (2016) 79-91.

[40] T. Wandowski, P.H. Malinowski., W.M. Ostachowicz, Circular sensing networks for guided waves based structural health monitoring, Mech. Syst. Signal. Pr. 66-67 (2016) 248-267.

[41] P. Hora, O. Cervena, Determination of Lamb wave dispersion curves by means of Fourier transform, App. Comput. Mech. 6(1) (2012) 5-16.

[42] B. Xu, L. Yu, V. Giurgiutiu, Advanced Methods for Time-Of-Flight Estimation with Application to Lamb Wave Structural Health Monitoring, The 7th International Workshop on Structural Health Monitoring - 2009, Stanford University, Palo Alto, CA.

[43] L. Maio, F. Ricci, V. Memmolo, E. Monaco, N.D. Boffa, Application of laser Doppler vibrometry for ultrasonic velocity assessment in a composite panel with defect, Compos. Struct. 184 (2018).

[44] L. De Marchi, J. Moll, A. Marzani, A Sparsity Promoting Algorithm for Time of Flight. Estimation in Guided Waves - Based SHM, Based SHM. EWSHM - 7th European Workshop on Structural Health Monitoring, IFFSTTAR, Inria, Université de Nantes, Jul 2014, Nantes, France.

Highlights

- Novel algorithm of damage detection and its size estimation based on guided waves has been developed
- The difference in the amplitudes and radiuses of wavefronts reflected from the end and middle damage point are presented
- The proposed approach allows for minimizing the extent of piezo transducer network

Beata Zima: Conceptualization, Methodology, Software, Visualization, Investigation, Data curation, Writing- Original draft preparation, Writing- Reviewing and Editing

Declaration of Interest:

Author declares no conflict of interest.

Ethical Statement:

Author states that the research was conducted according to ethical standards.